Title: **Grain Boundary Segregation in Iron Doped Strontium Titanate: from Dilute to Concentrated Solid Solutions**

Authors: Dylan Jennings[1,2], M. Pascal Zahler[1], Di Wang[3], Qianli Ma[1], Wendelin Deibert[1], Moritz Kindelmann[1,2,4], Christian Kübel[3,5], Stefan Baumann[1], Olivier Guillon[1,6], Joachim Mayer[2,4], and Wolfgang Rheinheimer[1,7,8]

1. Forschungszentrum Jülich GmbH, Institute of Energy and Climate Research, Materials Synthesis and Processing (IEK-1), 52425 Jülich, Germany
2. Forschungszentrum Jülich GmbH, Ernst Ruska-Centre for Microscopy and Spectroscopy with Electrons, Materials Science and Technology (ER-C 2), 52425 Jülich, Germany
3. Institute of Nanotechnology & Karlsruhe Nano Micro Facility, Karlsruhe Institute of Technology, 76344 Eggenstein-Leopoldshafen, Germany
4. Central Facility for Electron Microscopy (GFE), RWTH Aachen University, 52064 Aachen, Germany
5. Department of Materials & Earth Sciences, Technical University Darmstadt, 64287 Darmstadt, Germany
6. Jülich Aachen Research Alliance, JARA-Energy, 52425, Jülich, Germany
7. Institute of Mineral Engineering, RWTH Aachen University, 52064 Aachen, Germany
8. *Now at* Institute for Manufacturing Technologies of Ceramic Components and Composites, University of Stuttgart, 70569 Stuttgart, Germany

Abstract:

Strontium titanate, a perovskite oxide, is a frequently studied material for a large variety of applications. When acceptor-doped (with Fe, for example), the material is useful for its mixed oxygen and electronic conductivity, with potential use in oxygen transport membranes or as a cathode for solid oxide fuel cells. A barrier to conductivity in perovskites is the presence of space charge regions at the grain boundaries, which form due to the segregation of charged point defects. Typically, space charge theory assumes bulk dopant concentrations beneath the dilute limit, however concentrated solid-solutions are often utilized in applications. The current work aims to address this disparity: grain boundary segregation in strontium ferrite-strontium titanate solid-solutions is analyzed at three compositions, with Fe contents ranging from near the dilute limit to well above the dilute limit (Fe contents of 2%, 5%, and 25% on the B-site of the perovskite). Electrochemical impedance spectroscopy shows an increase in material conductivity as Fe is added. High-resolution STEM imaging and spectral mapping is utilized, showing that Fe segregates to the grain boundary core, contrary to what is expected from space charge theory. As the Fe content is increased, the amount of Fe segregated to the boundary increases significantly, but the segregation width of Fe at the boundary remains consistent.

Keywords: grain boundary segregation, strontium titanate, solid solution, STEM

1. Introduction

Perovskite oxides are a critical class of ceramic materials for a wide variety of applications, including many where ionic and/or electronic conductivity of the material is paramount[1–4]. Strontium titanate ($SrTiO_3$), a common perovskite, has been heavily studied, and is often doped at the B-site (Ti site) to achieve the preferred properties [5–8]. Acceptor doping (in particular, iron doping) of strontium titanate at levels above the dilute limit (usually expected to be around 1 at %) has proven to improve both the electric conductivity and the oxygen permeability of the material [9–13]. Given the impact of Fe doping on material properties, iron doped strontium titanate is of interest for a range of applications, including for oxygen transport membranes and solid oxide fuel cell cathodes [14–17]. In any application of polycrystalline ceramics, the properties of grain boundaries (GBs) will have an outsized impact on overall material performance. In many conducting ceramics, grain boundaries are typically expected to be blocking to conductivity due in part to the presence of space charge layers, arising from the segregation of charged defects to the grain boundary [18–25].

Space charge layers in doped strontium titanate have been thoroughly examined in the literature, particularly in the case of acceptor doping below the dilute solution limit [23–26]. It is well understood that grain boundaries in strontium titanate are positively charged due to the reduced Gibbs formation energy of oxygen vacancies (which are positively charged point defects, notated $V_O^{\cdot\cdot}$ in Kröger-Vink notation [27]) at the GB core [21,23,28]. As a result, a negatively charged space charge region (comprised of, e.g., strontium vacancies, V_{Sr}'', and iron substitutional defects, Fe_{Ti}') is expected to form adjacent to the boundary to compensate the core charge [21,23,26]. There are two widely used theories to describe space charge widths at grain boundaries: the Mott-Schottky (MS) and the Gouy-Chapman (GC) models [21,22,29–31]. Both the MS and GC space charge models take the assumption that only oxygen vacancies have a non-zero segregation energy to the grain boundary core [32]; therefore, the grain boundary core is positively charged and a negative space charge region forms adjacent to the boundary. In the MS model, oxygen vacancies are the only point defects which are assumed to be mobile, and in the GC model, both acceptor dopants and oxygen vacancies can redistribute to form the space charge region [21,29]. While there is evidence that the two models are

not accurate in certain cases [29,33], they are widely accepted descriptions of space charge behavior below the dilute solution limit.

Space charge layers are a result of the spatial inhomogeneity in the distribution of point defects in the material, so a detailed understanding of the overall defect chemistry of the material of interest is critical. Strontium titanate-ferrite (referred to as STF, with the chemical formula $SrTi_{1-x}Fe_xO_{3-x/2}$) is effectively a solid solution ranging between the two end compounds, $SrTiO_3$ and $SrFeO_{2.5}$ [34,35]. In addition to differences in chemistry, the end compounds have different crystal structures, as strontium ferrite typically maintains a brownmillerite structure, with the chemical formula $Sr_2Fe_2O_5$ [36,37]. In STF solid solutions with higher Fe content (30 at % Fe or greater at the B-site), short range defect clustering is expected to be present [36,37], and some evidence of longer range oxygen vacancy ordering has been shown to occur in the literature [38,39]. The standard defect chemistry approach to acceptor doping of strontium titanate assumes the incorporation of Fe into the lattice as a negatively charged point defect onto the cation sublattice (Fe'_{Ti}, assuming Fe^{3+}). However, in the context of a concentrated solid solution, treating Fe as a constituent of the native lattice is a more accurate way to represent the defect chemistry of the system [10,34,35,40].

Experimental studies in Fe doped $SrTiO_3$ below the dilute limit has shown that cationic segregation tends to fit with expected space charge widths (~10-20 nm) [41–45]. However, many technologically relevant applications of STF involve doping at levels well above the dilute limit [10], where there is a lack of understanding of space charge behavior and dopant segregation at grain boundaries. While grain boundary segregation in concentrated solid-solutions has not been examined in STF, a variety of theoretical and experimental work has examined segregation behavior in concentrated solid solutions in other material systems; a variety of ion conducting ceramics, such as ceria and barium zirconate, are commonly doped at levels well above the dilute limit, and segregation widths at grain boundaries in these materials have been observed to be anywhere from 2 to 10 nm depending on the study [20,23,46–48]. Additionally, multiple theoretical approaches have been utilized to examine the effect of an increasing carrier concentration, indicating that segregation behavior and space charge widths change significantly as dopant concentration is increased [33,49,50].

While there is a robust literature of nanoscale analyses of dopant segregation at grain boundaries in strontium titanate, there are major gaps that the current study aims to address. Firstly, there is a lack of experimental evidence of how grain boundary segregation and space charge layers change when moving from a dilute to a concentrated solid solution. Additionally, many of the analyses of dopant segregation at grain boundaries in the literature do not reach spatial resolutions high enough to fully understand the segregation behaviors which are present. Finally, the grain boundary chemistry of concentrated STF solid solutions has yet to be defined, despite the technological relevance of the material. In the current work, three different STF compositions (in addition to an undoped $SrTiO_3$ control sample) are analyzed by electrochemical impedance spectroscopy and scanning transmission electron microscopy (STEM), with Fe contents ranging from near the dilute solute limit (2 at% Fe on the B-site, or 0.4 at% total) to well above the limit (25 at% on the B-site, or 5 at% total). Space charge layer widths are indirectly measured with EIS for all compositions, and grain boundary segregation is characterized with STEM at high spatial resolutions. In combination, the two techniques allow for a detailed understanding of how ionic segregation and space charge behavior transform based on Fe content. Particular emphasis is placed on characterizing and understanding the grain boundary chemistry of the material with the highest iron content (25 at% on the B-site). In total, the current work presents a detailed picture of grain boundary segregation behavior in STF, covering a significant compositional range.

2 Experimental

2.1 Powder Processing and Sample Preparation

Four total samples have been characterized in this work: three STF materials with different B-site iron contents (2 at %, 5 at %, and 25 at %), in addition to one undoped $SrTiO_3$ as a control. The current study compares grain boundary segregation behavior in samples from multiple other studies, so the preparation procedure varies slightly across samples. The as-synthesized chemical formulas for each sample analyzed are as follows: $SrTiO_3$, $SrTi_{0.98}Fe_{0.02}O_{3-\delta}$, $SrTi_{0.95}Fe_{0.05}O_{3-\delta,}$ and $Sr_{0.97}Ti_{0.75}Fe_{0.25}O_{3-\delta}$. From this point forward, the samples will be referred to using their B-site iron contents, with the following notation: undoped, 2% Fe, 5% Fe, and 25% Fe. All powders were

prepared using a mixed oxide/carbonate method. The undoped and 2% Fe powders were prepared with the following procedure: Stoichiometric powders were synthesized with a mixed oxide/carbonate method, using $SrCO_3$ (≥99.9%, Merck, Darmstadt, Germany), TiO_2 (rutile, ≥99.9%, Sigma Aldrich, St Louis, United States), and Fe_2O_3 powders (γ-Fe_2O_3, ≥98%, Alfa Aesar, Ward Hill, United States). The powders were ball milled with isopropanol and 3 mm diameter ZrO_2 milling balls using a PM400 planetary ball mill (Retsch, Haan, Germany) for 15 cycles of 5 min at 400 rpm. Powders were sieved and calcined at 975 °C for 3 h, and then were milled again for 6 cycles of 5 min at 300 rpm. Green bodies were uniaxially pre-pressed and then cold-isostatically pressed at 400 MPa. Sintering was done in air, with sintering conditions selected to optimize for sample density and phase purity. The undoped sample was sintered at 1425 °C for 1 hour, and the 2% Fe sample was sintered at 1350 °C for 1 hour. The furnace ramp rates for the undoped and 2% Fe samples were set to 10 K/min.

The 5% Fe sample was also prepared with a mixed oxide/carbonate method, following the procedure from Zahler et al. [44]. The following raw materials were used: $SrCO_3$ (99.97%, Sigma Aldrich, St Louis, United States), TiO_2 (rutile, 99.997%, Sigma Aldrich, St Louis, United States), and Fe_2O_3 powders (98.1%, Merck, Darmstadt, Germany). Stoichiometric combinations of raw materials, along with isopropanol and 2 mm ZrO_2 balls, were attrition-milled for 4 h at 1000 rpm. The suspensions were then sieved and calcined for 6 h at 975 °C. The powders then were milled further in a planetary ball mill, with isopropanol and 10 mm zirconia balls, at 300 rpm for 16 h. Powders were again sieved and dried, and then pellets were uniaxially and cold-isostatically pressed (400 MPa) to form green bodies. The 5 % Fe green bodies were sintered at 1350 °C for 4 hours to attain the final sample.

The 25% Fe sample ($Sr_{0.97}Ti_{0.75}Fe_{0.25}O_{3-\delta}$) was synthesized from the raw materials $SrCO_3$ (Carl Jäger Tonindustriebedarf GmbH, Hilgert, Germany), TiO_2 (Alfa Aesar, Thermo Fisher (Kandel) GmbH, Kandel, Germany) and Fe_2O_3 (Kremer Pigmente GmbH & Co. KG, Aichstetten, Germany) by a solid-state reaction route. All starting powders were homogenized in a PE-bottle with 5 mm ZrO_2 milling balls and Ethanol with a 1:2:3 weight ratio. After 24 h on a rolling bench the mixture was dried and sieved with 500 µm mesh size. Subsequently, the raw powder mixture was calcined at 1100 °C for

5 h in a ZrO_2 crucible to form the perovskite STF25 phase. Tape-casting was performed on a micro-tapecaster (KaroCast 300–7, KMS Automation GmbH, Dresden, Germany). More details on the slurry preparation and components can be found elsewhere [51–53]. A casting speed of 5 mm/s and a blade gap of 900 µm was used to prepare the membrane layer. After drying of the tape, disk shaped samples were cut out of the tape and sintered at 1400 °C for 5 h in air. The furnace ramp rate was 5 K/min and dense ceramic samples were achieved. As tape-cast samples were too thin for impedance analysis, 25 % Fe containing green bodies for impedance were prepared by uniaxially pre-pressing and then cold-isostatically pressing at 400 MPa, and then were sintered at 1400 °C for 2 hours. The furnace ramp rate for impedance samples was 2 K/min.

2.2 Impedance analysis

The electric properties of each sample were measured by electrochemical impedance spectroscopy. Two different setups were used for impedance measurements: a high temperature and a low temperature setup, which could be cooled with liquid nitrogen. In both setups an Alpha-A high performance frequency analyzer (Novocontrol Montabaur, Germany) served as the measurement device. Undoped and 2 % Fe-doped $SrTiO_3$ samples were analyzed with the high-temperature setup between 400 °C and 600 °C in a frequency range of 10^{-1} Hz to 10^6 Hz. For samples with a higher Fe content (5 % and 25 % Fe), the low temperature setup was used in a temperature range from 25 °C to 150 °C with frequencies from 10^{-1} Hz to 10^7 Hz. All samples were contacted with platinum electrodes which were sintered at 900 °C in air for 2 h. Impedance data were fitted using the RelaxIS software (rhd instruments, Darmstadt, Germany). The equivalent circuits for fitting were designed based on the Brick-Layer model and made out of a series of RQ-Circuits, a resistor connected parallel to a constant phase element. The number of RQ-circuits (either 2 or 3) in the equivalent circuit was determined using a Distribution of Relaxation Frequency (DRT) analysis. The first of the circuits represents the grain bulk response, the second the grain boundary response and the third the electrode response, if visible. The fitting parameters (resistances and capacities) were then used in calculation of space charge layer widths and potentials.

The impedance fitting procedure is the same procedure as detailed in Zahler et al [54]. The capacities and resistances of both the grain boundaries and grains were attained by fitting the experimental impedance data (Figure 1), using an equivalent circuit based on the Brick-Layer model [55]. effective grain boundary conductivities (σ_{GB}) for each sample were calculated using the grain boundary capacities and resistances from impedance fitting (Equation 1). In Equation 1, $R_{GB,total}$ is the total grain boundary resistance, $C_{Bulk,total}$ and $C_{GB,total}$ are the total bulk and grain boundary capacities, l is the sample thickness and A is the cross-sectional area [56,57]. The value calculated in Equation 1 is an overall grain boundary conductivity for the full sample, so the term 'effective grain boundary conductivity' is used to describe σ_{GB} in the manuscript.

$$\sigma_{GB} = \frac{l}{A \cdot R_{GB,total}} \cdot \frac{C_{Bulk,total}}{C_{GB,total}} \qquad \textbf{Equation 1}$$

The space charge thickness has been calculated by the Mott-Schottky equation, shown in Equation 4 [26].

$$\lambda_{MS} = \lambda_{Debye} \cdot \sqrt{\frac{4e\Delta\Phi}{k_b T}} \qquad \textbf{Equation 4}$$

In Equation 4, λ_{Debye} is the Debye length of the space charge, e is the elementary charge, $\Delta\Phi$ is the space charge potential, k_b is the Boltzman constant, T is the temperature (in K) and λ_{MS} is the Mott-Schottky space charge layer width at the grain boundary. The Debye length is calculated according to Equation 5 [26].

$$\lambda_{Debye} = \sqrt{\frac{\epsilon_0 \epsilon_r k_b T}{2e^2 \cdot c_{major}}} \qquad \textbf{Equation 5}$$

In Equation 5, c_{major} is the concentration of the major defect in the system. Oxygen vacancies ($V_O^{\cdot\cdot}$) are assumed to be the major defects for the conditions during impedance measurements; their concentration is calculated based on the Fe dopant concentration in the samples ($2[V_O^{\cdot\cdot}] \approx [Fe'_{Ti}]$) [58] (with the exception of the undoped sample, where it was assumed that $[V_O^{\cdot\cdot}] \approx 10^{18}$ cm^{-3} [59]). Also required for solving Equation 4, the space charge potential ($\Delta\Phi$) can be obtained by numerically solving Equation 6 [60].

$$\frac{\tau_{GB}}{\tau_{bulk}} = \frac{\exp\left(\frac{e\Delta\Phi}{k_b T}\right)}{2e\Delta\Phi} \cdot k_b T \qquad \textbf{Equation 6}$$

In Equation 6, τ_{GB} and τ_{bulk} are the relaxation times of the impedance signal for the grain boundary and the bulk, respectively.

2.3 STEM, SEM, and XRD Characterization

Scanning electron microscopy (SEM) analysis was performed using a Gemini G450 FEG-SEM (ZEISS, Oberkochen, Germany) with a backscattered electron detector. Grain size measurements were done using the linear intercept method. X-ray diffraction (XRD) patterns for each sample were collected with a D4 Endeavor XRD device (Bruker, Billerica, United States). Scanning transmission electron microscopy (STEM) data from all samples was collected using multiple instruments. An HF5000 STEM (Hitachi High-Technologies, Tokyo, Japan) was utilized for imaging and energy dispersive x-ray spectroscopy (EDS) mapping of the undoped, 5% Fe, and 25% Fe samples. A Themis-Z (Thermo Fisher Scientific, Waltham, United States) was utilized for STEM analysis of the 2% Fe sample, and a Titan G2 80-200 CREWLEY [61] (Thermo Fisher Scientific, Waltham, United States) was used for analysis of the 25% Fe sample (including high resolution (HR) STEM, EDS mapping, and electron energy loss spectroscopy (EELS) mapping). Samples for STEM analysis were prepared by two methods: a conventional TEM preparation method and a focused ion beam (FIB) lift-out method. For TEM samples prepared conventionally, sintered ceramics were cut and dimpled before being ion polished using a PIPS II ion mill (Gatan, Pleasanton, United States), with a final milling energy of 200 eV. For samples prepared using the FIB, a Helios NanoLab 460F1 FIB-SEM [62] (Thermo Fisher Scientific, Waltham, United States) was utilized, with a final milling energy of 2 KeV. EDS mapping in the SEM was also done using this FIB-SEM. Select FIB samples were polished further utilizing a model 1040 NanoMill (E.A. Fischione Instruments, Export, United States), using a final milling energy of 500 eV.

STEM spectral data (EDS and EELS) was analyzed using HyperSpy [63]. EDS maps at medium to low magnification (Figures 2(a), 3(a), 4(a), and 5(a)) were quantified using a standard-less (Cliff-Lorimer) quantification, with k-factors calculated by assuming the overall composition of the

map as equivalent to the as-synthesized material composition. The EDS quantification does not consider effects such as absorption and channeling, so errors above 5 % are anticipated [64,65]. High resolution EDS maps are not quantified (Figures 2(c), 3(c), 4(c), and 5(c)), with the exception of the off-zone map in Figure 6. Line scans were taken from the spectral images by first binning pixels into a line scan, then applying a quantification to the binned line. EDS maps were pre-filtered with a flat filter, to reduce noise while preventing the appearance of artifacts due to the filtering process. While EDS results are presented for the elements present in the samples (Sr, Ti, Fe, and O), it is important to note that the oxygen signal is (relative to that of the cationic species) considered to have larger error, as electron irradiation in the TEM has been shown to induce reduction in oxides [66,67]. HRSTEM images were denoised utilizing a nonlinear filtering algorithm developed for use on HRS/TEM micrographs [68].

Where necessary, sample thicknesses was measured using EELS, assuming a mean free path of 100 nm, with an anticipated error of around 20% [69]. Full-width-at-half-maximum (FWHM) values for Fe segregation at several grain boundaries are reported, with errors calculated using the residuals of a gaussian fit to the data. The ratio of Fe grain boundary content to the bulk has also been reported for several grain boundaries, where errors are propagated from the difference in bulk Fe content on either side of the grain boundary. The Fe content and FWHM are also reported for the three different Fe containing samples, along with error bars, which were calculated using the same method as above. The 5% and 25% Fe data points for segregation width and Fe content are an average of two and three GBs, respectively, so error propagation was done for those data. Samples with higher Fe contents showed inhomogeneities in Fe distribution. To allow for comparison between samples, only grain boundaries showing ‘symmetric’ segregation at lower magnification (i.e. where the grain bulk on both sides of the boundary looked to have similar composition) were chosen for analysis at high resolution. Excess Fe at the GB (in atoms/nm^2) was calculated using the spatial difference method [70,71], with error bars taken to be the standard error of the mean.

STEM HAADF image and EDS map simulations were performed with muSTEM [72]. To closely approximate an experimental grain boundary from the 25% Fe containing sample, a supercell

consisting of 9015 atoms was built. To replicate the experiment, the sample thickness for simulations was set to be 75 nm, and the STEM convergence angle was set to 24.7 mrad. The HAADF detector collection angle was set to be 70-200 mrad. In the experimental case, the grain boundary is between two grains, one which is oriented along a ⟨100⟩ type zone, and the other which is oriented between a ⟨310⟩ and a ⟨210⟩ zone. As an approximation, the model grain boundary consists of one grain aligned along a ⟨100⟩ type zone axis, and the other grain oriented along a ⟨210⟩ zone. The faceting of the boundary in the model was made to replicate the experimental HAADF image. The mixed B-site chemistry of STF was simulated by setting the fractional occupancy of each B-site atom in the simulation (i.e. each B-site was assumed to be partially occupied by Fe and Ti). The chemistry of each grain was varied adjacent to the grain boundary, with the first B-site plane adjacent to the boundary consisting of 87% Fe, and the second B-site plane from the boundary consisting of 74% Fe. In addition to changes in B-site chemistry, some Sr deficiency was included in the first A-site plane adjacent to the boundary, assuming an occupancy of 80% Sr. To account for the disordered nature of the GB, random displacements were added to the three planes with altered chemistry. Displacements 10 times the amplitude of the standard thermal vibrations added to the first B-site plane, and displacements 5 times the amplitude of thermal vibrations were added to the other two planes. Due to the high levels of Fe segregation at the grain boundary, the chemistry of the bulk in the model was assumed to be 80% Ti and 20% Fe (slightly Fe depleted relative to the as-synthesized composition). As a result of the large super-cell size, the absorptive model was used to account for thermal scattering, reducing the calculation time. The simulation result was convolved with a gaussian with a sigma of 0.14 nm to account for the size of the electron beam. Grain boundary models for EDS simulations and figures were prepared utilizing VESTA [73].

3 Results

3.1 Microstructural Analysis

The microstructures of sintered samples were characterized by either SEM or low-magnification STEM imaging, depending on grain sizes (Figure S1). Additionally, X-ray diffraction patterns from each sample were produced to check phase purity (Figure S2). A general trend in grain

size can be seen in Figure S1, where grain sizes decrease as the Fe content in the samples increases. The measured average grain sizes are as follows, from lowest to highest Fe content: 4.5 μm, 1.1 μm, 0.2 μm, and 0.7 μm. Samples look to be fully dense and homogeneous when viewed with SEM and STEM. The XRD results (Figure S2) indicate that all samples maintain a perovskite crystal structure, and the undoped, 2% Fe, and 5% Fe samples are all shown to be free of secondary phases. The XRD pattern of the 25% Fe containing sample indicates that some secondary phases are present, which were confirmed to be iron oxide by SEM imaging and EDS mapping (Figure S3). The incomplete mixing of Fe into the 25% Fe sample is expected to be a result of kinetic limitations related to the processing of the material, not a result of a thermodynamic barrier to forming a solid-solution. The distance between secondary phases is shown to be fairly large (hundreds of microns), so STEM samples were prepared to avoid the iron oxide phases. Based on microstructural characterization, the samples of each composition were determined to be high enough quality for detailed EIS and STEM analyses.

3.2 Electrochemical Impedance Spectroscopy

To assess the impact of Fe doping on material conductivity, electrochemical impedance spectroscopy was performed on the four samples of different compositions (undoped, 2 % Fe, 5 % Fe, and 25 % Fe). Figures 1(a) and 1(b) show representative Nyquist plots at either 550 °C or 150 °C for each material composition; the Nyquist plots of the four samples are reported at different temperatures so that the majority of the impedance response can be seen for each sample (refer to Figure S4). Fe doped strontium titanate is a mixed oxygen and electronic conductor, so under certain conditions mixed conduction would need to be considered when fitting Nyquist plots. However, literature strongly indicates that all Fe-containing samples are well into the p-type conduction regime in the conditions of this study (in air, T < 600 °C) [10]. The Nyquist plots for the undoped and 2% Fe samples were fit with two semicircles attributed to the sample: one representing the grain boundary contribution and one the grain bulk contribution. However, the grain boundary and bulk conductivities of the 5% and 25% Fe containing samples could not be reliably separated with this method, and therefore are not reported here (see Figure S4 and Table S1 for details). It should be noted that, due to the mixed-conducting nature of Fe-doped strontium titanate, the current analysis presents only a slice of the

electrical properties of the highly Fe-doped strontium titanate; a complete electrical characterization would require additional pO_2 dependent studies of the material.

A table of relevant fitting parameters for Figures 1(a) and 1(b) is included in the supplementary information (Table S1), showing that capacitance values for grain and grain boundary semicircles fit with expected values for electroceramics [74]. The Nyquist plots (Figures 1(a,b)) and a plot of total conductivity (Figure 1(c)) show that the increase in Fe content correlates to a decrease in resistivity. Bulk and effective grain boundary conductivity was extracted from the data for each sample composition, and is plotted in Figure 1(c), clearly showing an increase in both bulk and effective grain boundary conductivity as Fe content increases.

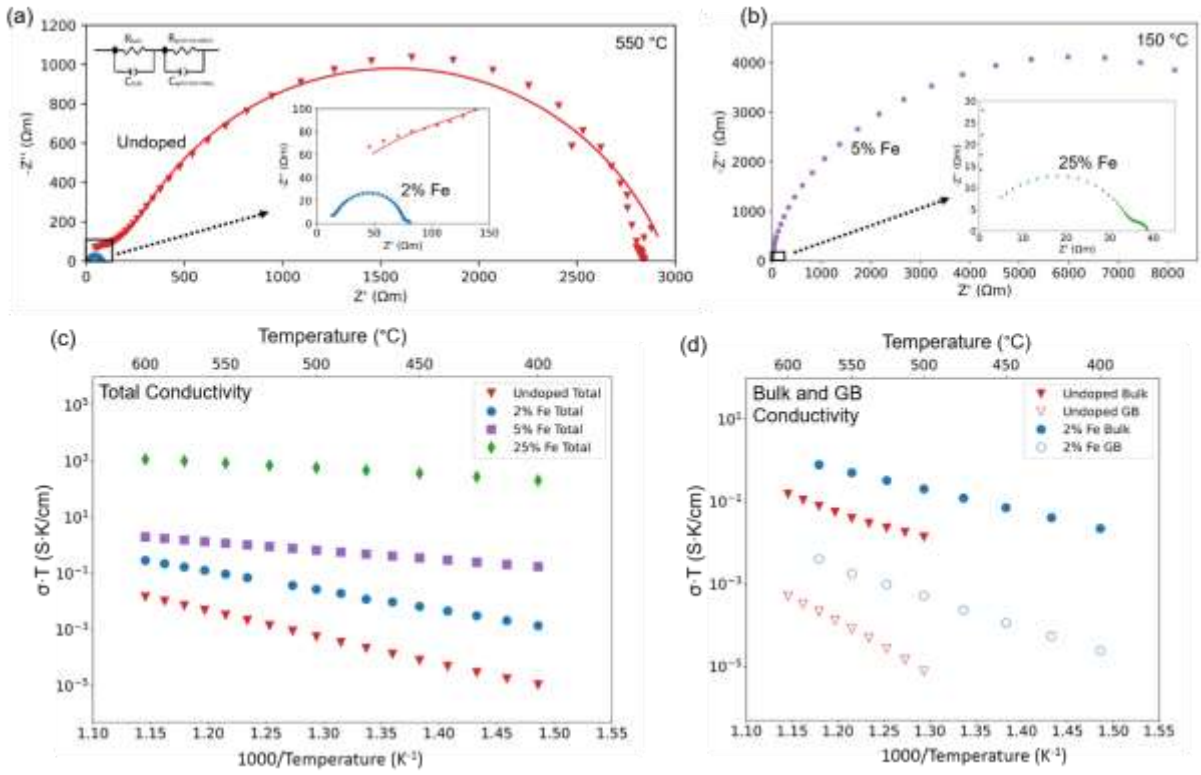

Figure 1: Electrochemical impedance spectroscopy results from the four samples in this work. (a) Representative Nyquist plots for the undoped and 2 % Fe samples, measured at 550 °C, and (b) Nyquist plots for the 5% Fe and 25% Fe samples, measured at 150 °C. The data points in (a,b) are measured data, and the solid lines in (a) represent the fit curves. The equivalent circuit used for fitting the sample components is notated in the upper left corner of (a). (c) Total conductivities for all samples measured over the same temperature range. (d) Bulk and effective grain boundary conductivity measurements for the undoped and 2% Fe doped samples. Bulk and GB conductivities could not be reliably separated for the samples with higher Fe contents. Note, the 525 °C data for the 2% Fe sample in (c) was lost during acquisition.

A Mott-Schottky effective space charge thickness was calculated from the impedance data (Table 1), indicating that an addition of Fe content results in a decrease in the Mott-Schottky barrier thickness. It is critical to note that the Mott-Schottky calculation is only valid for dopant concentrations below the dilute limit (which may not be the case for the 2% Fe sample); it is presented here to demonstrate that space charge thicknesses are expected to decrease significantly as Fe is added to the system. While the space charge 'thickness' reported in Table 1 provides a physical value, the correlation between the calculated Mott-Schottky thickness and dopant segregation is unclear [29]. Other approaches, such as the restricted equilibrium model [29,31], are more accurate, and are discussed in further detail in Section 4. Outside of defect interactions, other sources of error (such as how mobile charge carrier concentrations are calculated) will be impacting the higher Fe content samples. A more sophisticated analysis for addressing concentrated solid-solutions has been presented in the literature [49], but was considered to be outside of the scope of this work. While the Mott-Schottky barrier thickness could not be determined for the 5% and 25% Fe containing samples, the space charge layer thickness is expected to continue to decrease as additional acceptor dopant is added to the system [49].

Table 1 also details the activation energies for the bulk and the effective grain boundary conductivities of the two samples which could be fit from the data in Figure 1(d). Activation energies are lower for bulk conductivity than for effective grain boundary conductivity, though the difference shrinks as Fe is added. Both bulk and GB activation energies decrease going from undoped to Fe-doped.

Table 1: Activation energies and Mott-Schottky space charge thicknesses calculated from EIS results

Fe content (% of B-site)	Bulk E_A (eV)	GB E_A (eV)	Mott-Schottky Thickness (nm)	Temperature Range of Fit (°C)
undoped	1.43	2.46	45.8	500 – 600
2	1.04	1.45	4.7	400 – 575

The difference between effective grain boundary conductivity and bulk conductivity is observed to increase as Fe is added, indicating that GBs are becoming less blocking to conductivity, and total conductivity increases as the Fe content is increased. Additionally, the Mott-Schottky

thicknesses are expected to decrease as additional Fe is added, so classical space charge theory would predict that a corresponding decrease in dopant segregation widths should occur. To fully understand the correlation between conductivity and nanoscale segregation behavior, each of the four samples which were analyzed by EIS were also analyzed by STEM/EDS, both at low magnification (i.e. not-atomic resolution) and high magnification (i.e. atomic resolution).

3.3 Segregation in Nominally Undoped Strontium Titanate

Nominally undoped strontium titanate was synthesized as a control sample to compare with Fe doped material. A general grain boundary in undoped strontium titanate was analyzed by STEM/EDS, at both low and high resolution, as seen in Figure 2. A quantified EDS mapping (in atom %) of a grain boundary at low resolution is shown in Figure 2(a), and an integrated line-scan across that boundary is shown in Figure 2(b) with the grain boundary region highlighted in gray. The low-resolution EDS mapping and line scan clearly shows an increase in the concentration (relative to the other elements) of titanium and oxygen local to the grain boundary, while there is a decrease in the strontium content at the grain boundary. Analysis of an undoped grain boundary at high resolution was also done, including HRSTEM imaging (Figure 2(c)) and EDS mapping (Figure 2(d)). The HRSTEM imaging in Figure 2(c) shows a general grain boundary, with one grain aligned along a ⟨100⟩ zone axis, and the other misaligned. EDS intensity mapping from the area in the white box in Figure 2(c) indicates that the strontium depletion is localized to the grain boundary core region, with a measured FWHM of strontium depletion of 1.3 nm.

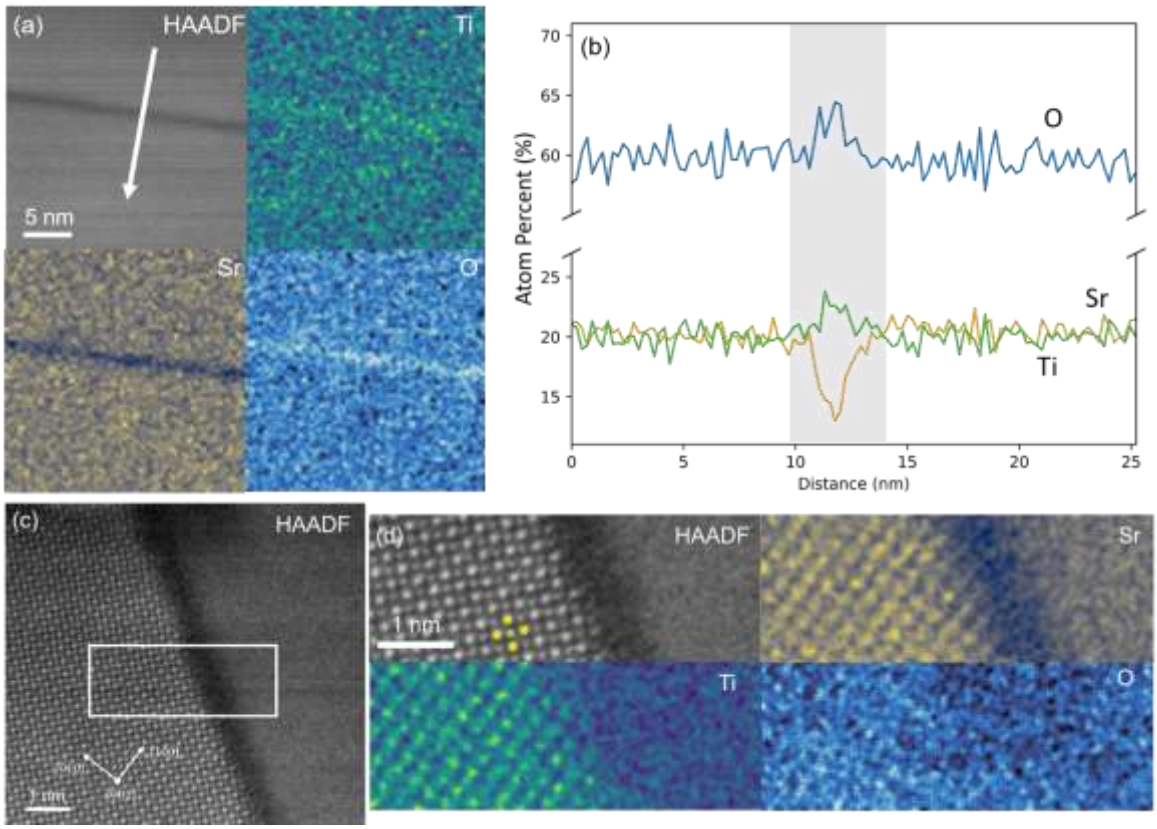

Figure 2: Low and high-resolution analysis of GB segregation in the undoped sample. (a) EDS mapping of general grain boundary in undoped STO. (b) Line scan of EDS mapping in (a), showing elemental segregation around the grain boundary (gray highlighted region). (c) HRSTEM HAADF image of a general grain boundary in undoped strontium titanate. (d) EDS map of the area within the white box in (c), showing strontium depletion at the grain boundary. One unit cell is overlaid in (d), indicating positions of Sr (yellow) and Ti/O (green) columns. (a) and (b) are reprinted, with permission from Elsevier, from the Journal of the European Ceramic Society, Volume 43: M.P. Zahler, D. Jennings, M. Kindelmann, O. Guillon, and W. Rheinheimer, *Reactive FAST/SPS sintering of strontium titanate as a tool for grain boundary engineering*, 6925-6933, 2023. [54]

3.4 Segregation near the dilute solution limit

The lowest Fe content analyzed in the current study is 2% Fe (i.e. 2% Fe on the B-site of the perovskite, or 0.4 at% Fe in total), which is expected to be near the dilute solution limit. As with the undoped strontium titanate in section 3.3, segregation behavior in the STEM was analyzed in the 2% Fe doped material at both low and high resolution. In Figure 3(a), a low magnification (quantified) EDS map of a triple junction is presented, showing clear Fe segregation and Sr depletion at the grain boundary. At this composition, there is no clear titanium segregation nor depletion at the grain boundary. This is also shown in the linescan in Figure 3(b), which is taken across a single grain

boundary (with the GB region highlighted in gray) from the line drawn in Figure 3(a). The segregation width of Fe at this grain boundary has a FWHM of 9 nm. A grain boundary in the same sample was also chosen to be analyzed by HRSTEM/EDS. Figure 3(c) shows a high-resolution STEM image of a grain boundary which looks to be at (or very close to) an edge-on condition. The grain on the right side of Figure 3(c) is aligned down a ⟨110⟩ type zone axis, while the left-hand grain is misaligned, but a set of {100} planes are close to alignment. EDS intensity mapping in Figure 3(d) indicates that the Fe segregation and Sr depletion are actually highly localized to the grain boundary, only spreading 1-2 unit cells outside of the grain boundary core region (the FWHM of Fe segregation was measured to be 1.5 nm). The measured segregation width at low magnification is anticipated to be impacted significantly by the large pixel sizes, grain boundary tilt away from an edge-on condition, and imprecise beam positioning, so the high-magnification EDS mapping will give a much more precise picture of grain boundary segregation widths.

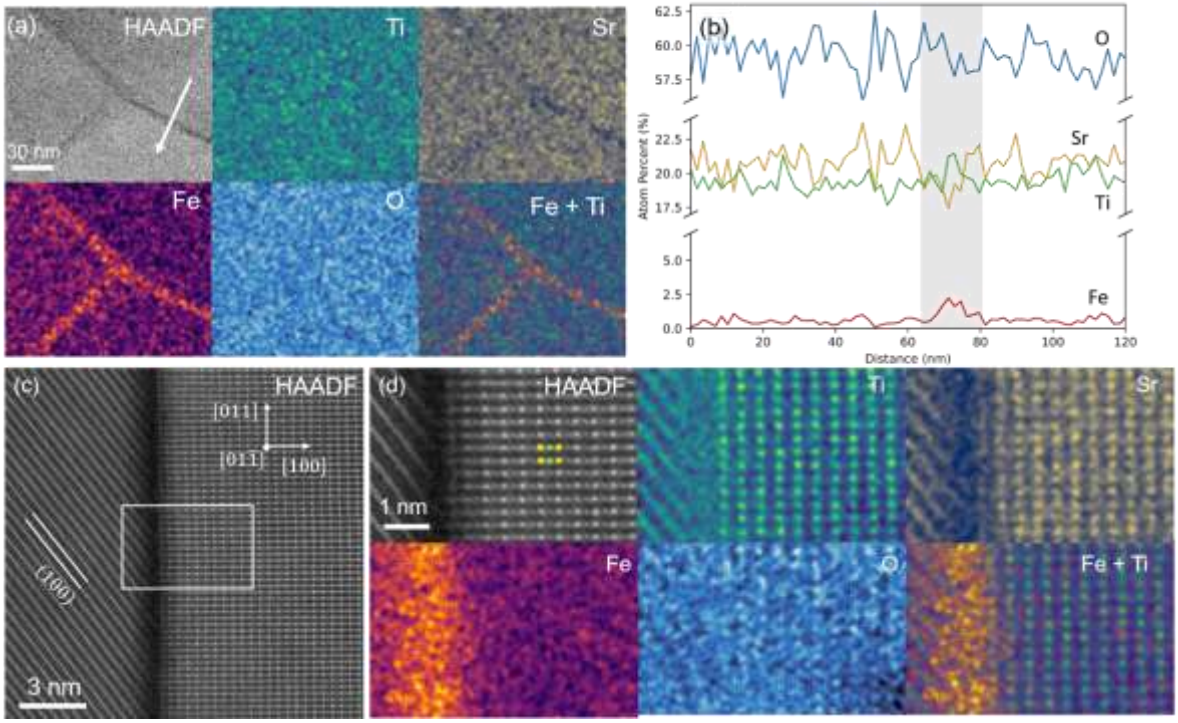

Figure 3: Low and high-resolution analysis of GB segregation in the 2% Fe sample. (a) Low magnification EDS mapping of a triple junction in 2% Fe doped strontium titanate, showing segregation of Fe to the grain boundaries of the material. (b) A line scan across one of the boundaries in (a) (the direction of which is indicated by the white arrow) shows the segregation behavior at the grain boundary (highlighted in gray). (c) High resolution HAADF image of a grain boundary in 2% Fe doped STO. (d) EDS mapping from the white area in (a), showing that Fe segregation is confined within 1-2 unit cells from the grain boundary core.

3.5 Segregation slightly above the dilute limit

The intermediate Fe level which was studied, at an Fe content of 5% at the B-site (1 at% total), contains an amount of Fe which is expected to be into the concentrated solid-solution regime. In the manner of the other compositions studied, elemental segregation in the 5% Fe sample was studied by STEM/EDS at both low and high resolution, as shown in Figure 4. Low-resolution EDS mapping (Figure 4(a)) indicates that significant inhomogeneity in the B-site cation distribution exists in the sample both within and between grains. Grain boundaries display clear Fe segregation, without any obvious Ti segregation or depletion at the boundaries, closely matching the result from the 2% Fe doped sample. Additionally, there are some grain boundaries which have a sharp, symmetrical Fe segregation, while others have a more blurred profile. The causes of the inhomogeneity outside of the GB regions is unknown, but could be a result of a solute drag effect, as has been shown in the literature with this material [44]. For consistency, and to allow for comparisons between samples, only grain boundaries with sharp, symmetrical segregation profiles were chosen for high resolution analysis.

The Sr map does not show any depletion at the grain boundary at low resolution, contrary to what is observed in the undoped (Figure 2) and 2% Fe doped (Figure 3) samples. An integrated line scan across one of the grain boundaries in Figure 4(a) (indicated by the white arrow) is shown in Figure 4(b), with the grain boundary region highlighted in gray, showing the clear increase in Fe content without much noticeable segregation or depletion in the other atomic species. A high-resolution HAADF image of a grain boundary is shown in Figure 4(c), and EDS intensity mapping from that image is presented in Figure 4(d). The high-resolution EDS map (Figure 4(d)) clearly shows that the Fe segregation is limited to ~1 nm on either side of the grain boundary core (the measured FWHM of Fe segregation is 1.2 nm). Additionally, Ti and Sr depletion at the grain boundary are noticeable at high resolution, despite not being visible in the lower-magnification mapping.

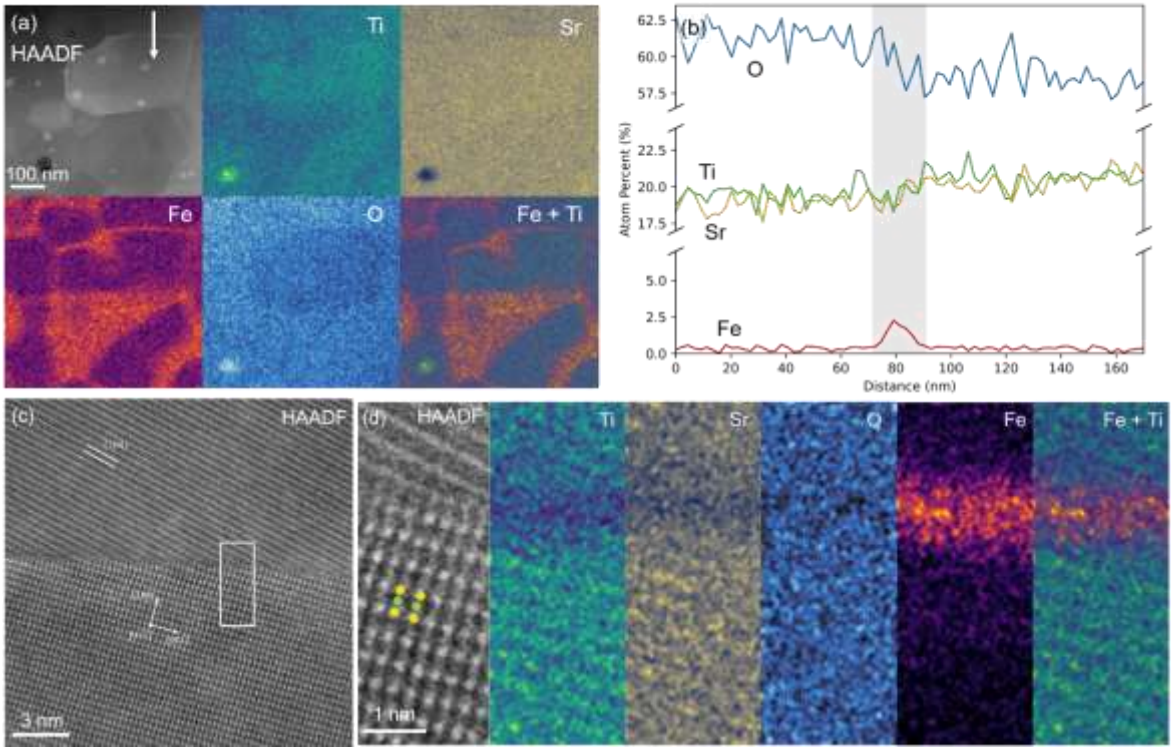

Figure 4: Low and high-resolution analysis of GB segregation in the 5% Fe sample. (a) HAADF imaging and EDS mapping at low magnification for a 5% Fe content STF sample. (b) Linescan across a grain boundary from (a) (indicated by the white arrow), showing Fe segregation at the grain boundary (highlighted in gray) in the material. (c) High resolution HAADF imaging and (d) EDS mapping (of the area inside of the white rectangle in (c)) of a single grain boundary, showing segregation to the grain boundary core. Sr (yellow) and Ti (green) column positions are marked in the image in (d).

3.6 Detailed analysis of segregation well above the dilute limit

The final STF composition studied contained an Fe content of 25% on the B-site, or 5 at% total. For better sintering and phase stability the sample was prepared to be A-site deficient (the ratio of A-site to B-site cations is 0.97), so the overall as-prepared Fe content is actually slightly higher than 5 at%. At this composition, the material is anticipated to be well above the dilute limit, ergo firmly in the range of a concentrated solid-solution. Given that there is a lack of S/TEM analysis of chemical segregation of concentrated STF solid solutions, more effort was put forth in characterizing the 25% Fe sample as compared to the other three compositions. To facilitate a direct comparison to the other compositions, low- and high-resolution EDS mapping was performed with the 25% Fe sample (Figure 5). The low-resolution mapping in Figure 5(a) clearly shows significant inhomogeneity in the B-site cation

distribution, on similar scale to what is observed in the 5% Fe containing sample (Figure 4(a)). Fe segregation and Ti depletion at the grain boundaries can be observed and large patches of Fe rich/Ti deficient regions within grains are visible in Figure 5(a). The patches of increased Fe tend to reside in the center of the grains, supporting the hypothesis that the inhomogeneity is resulting from solute-drag during sintering. As with the 5% Fe doped sample, to allow for comparisons between samples, grain boundaries with sharp, symmetrical segregation profiles were selected for high resolution analysis.

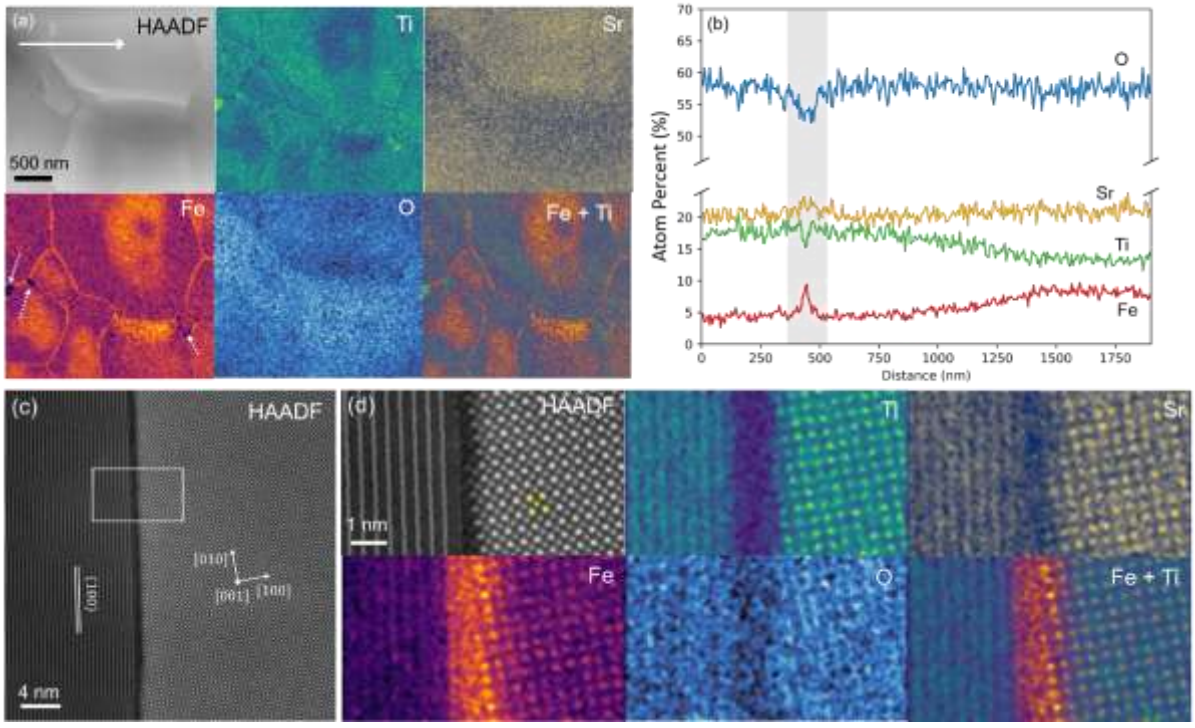

Figure 5: Low and high-resolution analysis of GB segregation in the 25% Fe sample. (a) HAADF imaging and EDS mapping of multiple grains in the Fe rich (25% Fe on the B-site) composition, showing significant inhomogeneity in the distribution of B-site cations. (b) Linescan across one grain boundary into a grain, showing segregation at the GB (highlighted in gray) and significant compositional changes within the grain (right side of the linescan). (c) HR HAADF imaging and (d) EDS mapping of a grain boundary within the 25% Fe sample, showing clear replacement of Ti with Fe in the vicinity of the grain boundary.

XRD and SEM of this sample (Figures S2 and S3) indicate that some secondary iron oxide phases are present, but no clear non-perovskite phase was observed in the STEM analyses which were performed on the sample. The only notable 'second phase' observed in STEM is a series of grains ~50 nm in diameter, which contain almost no Fe content (dashed arrows in Figure 5(a)). From EDS analysis, these grains look to be strontium titanate with a relatively low Fe content compared to the

majority of the grains in the sample. An integrated line scan across a section of the EDS map in Figure 5(a) is presented in Figure 5(b), clearly showing the increase in Fe at the grain boundary (highlighted in gray) and also a change in B-site composition within the right-hand grain. Additionally, the Fe segregation within the grain (right hand side of the line plot in Figure 5(b)) looks to be at a similar level as compared to the Fe peak at the grain boundary.

At high resolution, the grain boundary segregation behavior of the 25% Fe doped sample becomes clear. Figure 5(c) shows a high resolution HAADF image, with the right-side grain aligned down the [001] zone axis, and the left side grain aligned between the [013] and [012] zones, parallel to the (100) planes in the crystal. An EDS intensity map from the white box in Figure 5(c) is displayed in Figure 5(d), where Fe can be seen segregating to the grain boundary, replacing Ti on the B-sites of the perovskite. The EDS map also shows that Fe segregation follows the faceting of the grain at the boundary, with Fe content being highest on the first plane adjacent to the boundary. In addition to Fe segregation and Ti depletion at the grain boundary, Sr and O depletion are also present (but are less pronounced than the other two effects). The Fe content at the grain boundary in the 25% Fe sample is clearly very high, but the segregation width remains quite thin, around 1-2 nm.

In an attempt to better understand the grain boundary segregation in the 25% Fe sample, two small sample tilts away from the zone axis were done (~2° in each direction), while maintaining the orientation parallel to the (100) set of planes, and the tilt which showed the thinnest segregation by EDS was chosen for analysis (see Figure 6). The tilting experiment was performed for two main reasons: tilting away from zone reduces electron channeling effects, resulting in more reliable quantification [75], and it helps to ensure that the grain boundary is as close to edge-on as possible, which is not trivial given the complex nature of general grain boundaries. The grain boundary from Figure 5(c,d) was tilted around the [100] axis of the right hand grain, resulting in the image seen in Figure 6(a). An EDS map was taken from the white box in Figure 6(a), as seen in Figure 6(b), and an integrated linescan was drawn over the interface in the direction of the white arrow in Figure 6(a), resulting in Figure 6(c). The linescan in Figure 6(c) shows that the Fe content in the grain boundary is more than four times that of the near-GB region. The ratio of Fe to Fe plus Ti was measured from

Figure 6(c), indicating that the Fe concentration reaches 87% on the B-site at the grain boundary. The segregation width in Figure 6 was measured to have a FWHM of 1.4 nm, similar to the widths measured from the 2% Fe and 5% Fe containing samples. The measured segregation width will be impacted by sample thickness due to beam spreading, and the thickness of the sample in Figure 6 was measured by EELS to be ~73 nm (relatively thick for this type of analysis). Accordingly, two other grain boundaries in thinner regions of the 25% Fe sample were analyzed by the same tilting method, which are shown in Figures S7 and S8. A summary of the relevant measurements for the grain boundary segregation behavior are described in Table 2.

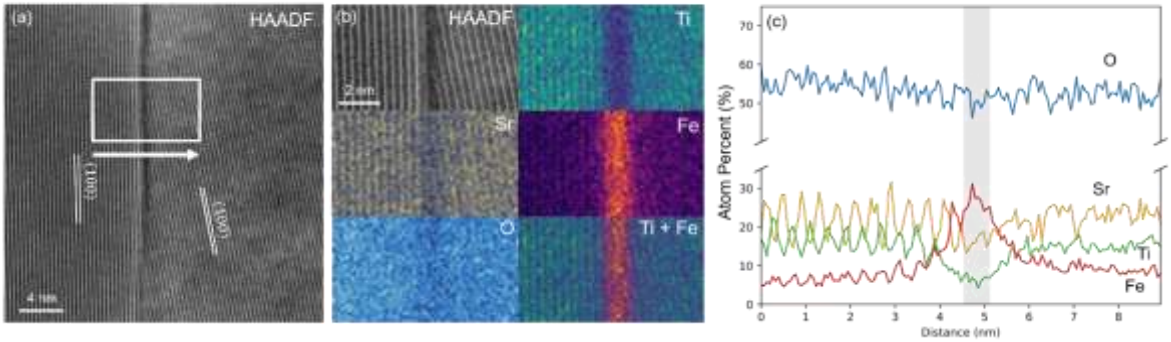

Figure 6: Off zone-axis HAADF imaging (a) of the same grain boundary as in Figure 5(c), with corresponding EDS mapping (b) of the white box in (a). A line scan (c) in the direction of the white arrow in (a) shows the quantified segregation behavior at the grain boundary (with the GB core region highlighted in gray). Tilting the sample off-zone reduces artifacts from electron channeling.

Table 2 allows for a comparison of the segregation behavior between three general grain boundaries in the 25% Fe sample. The TEM sample thickness varied between the three, from relatively thick for high resolution analysis (73 nm) to relatively thin (24 nm). The segregation widths (taken to be the FWHM of the line profiles) are similar between all three grain boundaries, with values in the range of 1.5 nm. Given the inhomogeneity in the 5% and 25% samples, it is difficult to say with confidence what the 'bulk' Fe content is in these two samples. To compare Fe content at the grain boundary, the ratio between Fe signal at the GB and near the GB reported in Table 2, which limits discrepancies in quantification between separate scans. The three grain boundaries show similar GB to near-GB Fe ratios, with a GB Fe content of about four times that of the region near the GB.

Table 2: Fe Segregation at three grain boundaries in the 25% Fe sample

Figure	Lamella Thickness (nm)	Segregation Width (nm)	GB to near-GB Fe ratio
6	73 ± 14	1.43 ± 0.11	4.2 ± 0.5
S7	45 ± 10	1.51 ± 0.05	4.0 ± 0.7
S8	24 ± 5	1.76 ± 0.16	3.8 ± 0.7

Electron energy loss spectroscopy (EELS) mapping was performed to analyze the chemistry near the grain boundary in the 25% Fe containing sample, as described in Figure 7. EELS mapping was done in the region of the grain boundary in Figure 7(a) defined by the white box (the grain boundary in Figure 7(a) is the same boundary as is characterized by EDS in Figure S7), and the EELS spectra were then binned parallel to the GB in the nine regions defined in Figure 7(a), with each binned region taken to encompass approximately one unit-cell in width. Noticeable in the Fe (Figure 7(b)) and Ti (Figure 7(c)) $L_{2,3}$ edges is the chemical segregation which was also seen by EDS, with the Fe peaks increasing in intensity considerably from position 1 to position 9, while the Ti peaks decrease in intensity over that same range. The Fe signal shows no significant change in shape or peak position, though a change in valency could be obscured by the low signal-to-noise ratio in the grain interior (a result of a lower Fe content in that region). The grain boundary from Figure 5(c) was also analyzed for changes in Fe valency at the boundary using EELS, but was also inconclusive with regards to changes in Fe peak position (Figure S9). The Ti signal in Figure 7, on the other hand, shows changes in both shape and position; the Ti $L_{2,3}$ spectra at positions 1-5 show crystal field peak splitting characteristic of Ti^{4+} in strontium titanate [76–79], but at the grain boundary (positions 6-9), the splitting is reduced and the peak positions shift to slightly lower energies (the L_2 peak position at the grain boundary is shifted by -0.55 eV compared to the near-GB). These two features together indicate a more disordered oxygen octahedral environment, and a reduction in Ti valency [76–79]. The O K spectra within the grain (positions 1-3 in Figure 7(d)) is typical for strontium titanate [77], showing three main peaks (indicated by the dashed lines in Figure 7(d)). At the grain boundary (positions 6-9), the two oxygen peaks at higher energy loss decrease in intensity and merge into one broad peak, a phenomenon that has been observed before in strontium titanate, and which is typically attributed to the breaking of the Ti-O bonding at the grain boundary (through the presence of oxygen vacancies at the boundary) [76,77,79].

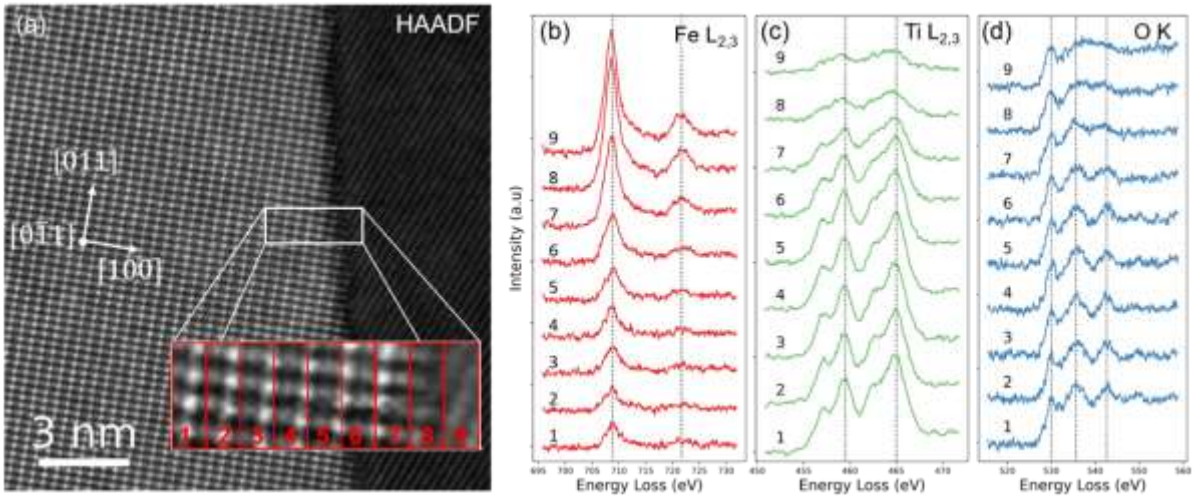

Figure 7: High resolution EELS analysis of Fe, Ti, and O at a grain boundary of the highly Fe doped (25% Fe on the B-site) strontium titanate. (a) HRSTEM HAADF image of a grain boundary (the same boundary as Figure S7), and EELS spectra from the nine binned regions in (a) for the Fe L edge (b), the Ti L edge (c), and the O K edge (d).

The EDS and EELS analysis presented of the 25% Fe containing sample allows for a close estimation of grain boundary chemistry. However, there are aspects of high-resolution spectral mapping (in particular, channeling and beam-spread) which are difficult to account for. To present a full model of the grain boundary chemistry in the 25% Fe sample, STEM HAADF and EDS simulations were performed, shown in Figure 8. The simulations were aimed at recreating the experimental result shown in Figure 5(d), allowing for a better atomistic description of the segregation behavior at grain boundaries in the 25% Fe sample. The experimental HAADF image of the grain boundary which is being modeled is shown in Figure 8(a), with the regions of modified chemistry highlighted. Based on the experimental EDS results from Figure 6 , a measurement was made that the peak Fe content at the grain boundary is 87% on the B-site, the Fe content one plane removed from the boundary is 74%. It was assumed that the segregation is limited to two unit cells on either side of the boundary. The GB model was made to represent this (Figure 8(b)), with the first B-site plane adjacent to the boundary (red) consisting of 87% Fe, and the second plane from the boundary (orange) being 74% Fe. Given that Sr depletion is also observed experimentally, the first Sr plane adjacent to the GB was assumed to be 80% Sr. The planes with altered chemistry also had some disorder introduced into the simulation to simulate structural disorder at the GB (see section 2.3 for details). Based on

measurements from Figure 6, the remaining lattice in the grain boundary model was assumed to have the composition of $SrTi_{0.8}Fe_{0.2}O_{3-\delta}$. For simplicity, no changes in the oxygen sublattice were made in the grain boundary model (the oxygen sublattice is not shown in Figure 8(b)).

The HAADF and EDS image simulations (Figure 8(d)) match well with the experimental results (Figure 8(c)), with clear Ti depletion and Fe segregation which follows the faceting of the grain boundary. The simulated and experimental HAADF images (Figure 8(d)) both show a decrease in contrast at the grain boundary. The simulated Fe EDS map still shows some regions with lower signal near the GB core which are not present experimentally, corresponding to the sections where the grain is Sr-terminated at the boundary. This disparity between simulation and experiment could be an indicator of a variety of different effects: there are expected to be steps in the grain boundary along the viewing direction, which are not easily visible experimentally, and no attempt at altering atomic positions around the grain boundary core was made. Additionally, some Fe could be residing on the A-site at the boundary, or additional Fe could be present in the GB core. Furthermore, the simulated EDS scan is free of the noise which is present in the experimental dataset. Overall, it should be noted that the model in Figure 8(b) is a simplified version of the real grain boundary, made to aid in a general understanding of GB chemistry in the 25% Fe containing material.

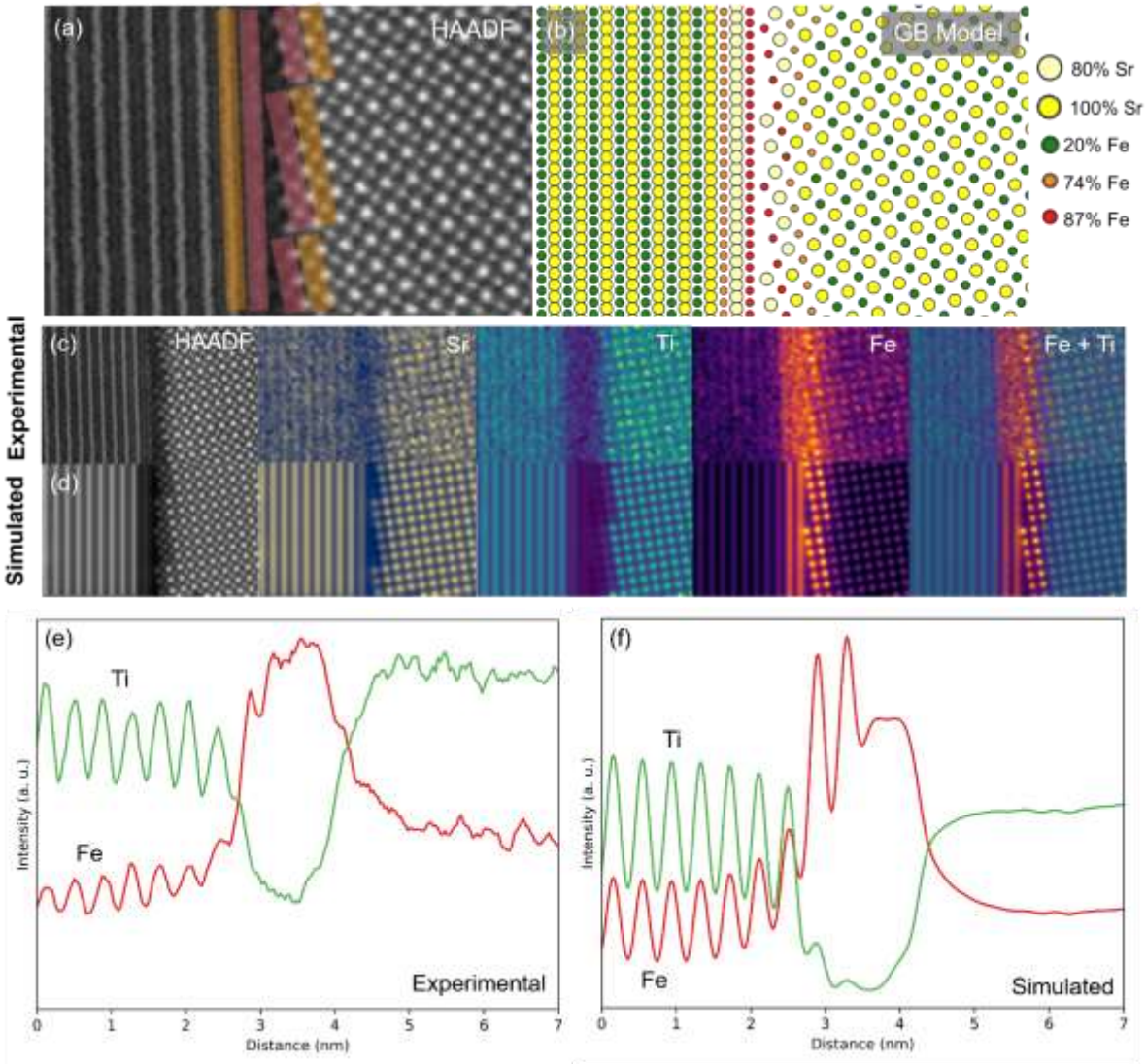

Figure 8: STEM image simulation results with the aim of understanding the true chemistry and structure of grain boundaries in the 25% Fe sample. (a) experimental HAADF image of the GB of interest, with the first adjacent unit cell (red), and second adjacent unit cell (orange) highlighted in the image. A model of the GB in (a) is presented in (b), assuming that the first adjacent B-site plane to the boundary is 87% Fe (red), and that the second adjacent plane is 74% Fe (orange). Additionally, the first A-site plane is assumed to be slightly Sr deficient (80% Sr). Some lattice disorder was added to the three planes with changed chemistry. The rest of the B-site sublattice in (b) is assumed to be 20% Fe. A comparison of the experimental (c) and simulated (d) HAADF images and EDS maps shows that the model boundary fits well with the experimental results. Integrated line-scans (from left to right) of the experimental (e) and simulated (f) b-site EDS signals show that segregation widths are successfully recreated by model.

A comparison of the experimental (Figure 8(e)) and simulated (Figure 8(f)) line scans of Ti and Fe signals also show a general agreement between the results. The impact of beam spread on the observed

segregation width can be seen clearly in the left side of the simulated line scan, which shows increased Fe signal in the three planes adjacent to the region of elemental segregation, and a similar effect can also be noticed in the experimental line scan. The Fe segregation width looks to be successfully recreated by the EDS simulation, supporting the hypothesis that segregation is effectively atomically sharp, being limited to only two unit cells on either side of the interface. The simulated line scan also supports what is observed in the simulated map, that some Fe signal near the GB core is not captured by the simplified GB model.

3.7 Comparison of Fe Segregation Behavior

As high-resolution S/TEM EDS analysis was performed for each sample (undoped, 2% Fe, 5% Fe, and 25% Fe), a quantitative comparison of the segregation behaviors between the samples can be done. Figure 9 describes two aspects of the segregation behavior which were determined to be most relevant, as a function of sample Fe content: Fe segregation widths (Figure 9(a)), and Fe concentration at the grain boundary (Figure 9(b)). While the results were analyzed with a quantitative method, it should be noted that there is a very limited sample for the measurements presented in Figure 9. The data in Figure 9 encompasses one grain boundary for the 2% Fe sample (Figure 3(c)), two for the 5% Fe sample (Figures 4(c) and S5), and three for the 25% Fe sample (Figures 6, S7, and S8). The FWHM of the gaussian fit of the Fe segregation profile was chosen as a quantitative representation of segregation widths in Figure 9(a). It is clear that there is no significant change in segregation width as a function of B-site cation concentration, with all values in the range of 1.3-1.6 nm. The low-resolution EDS line scans showed Fe segregation widths ranging from 9 nm (2% Fe) to 27 nm (25% Fe), demonstrating the importance of high-resolution analysis in accurate measurements of GB segregation. The disparity in segregation widths at low resolution is expected to be a result of several factors, including boundary mis-alignment and the large pixel dimensions of low-magnification spectral images.

In contrast to measured segregation widths, there is a significant difference in the Fe content at the grain boundary depending on the bulk Fe content, which is represented in two different ways in Figure 9(b). Given the inhomogeneity in the 5% and 25% samples, it is difficult to say with confidence what

the ‘bulk’ Fe content is in these two samples, so the data is described as Fe content in relation to the ‘near-GB’ region (taken to be the region of the high-resolution EDS scans furthest from the GB core). When considering the ratio of GB Fe intensity to near-GB intensity, the 2% and 5% Fe samples have the highest relative Fe content (around eight times higher than that of the near-GB region). The 25% Fe sample only has a GB Fe content around four times that of the near-GB region, however the difference is a result of the higher as-synthesized Fe content. When representing the data as B-site Fe concentration at the GB, the data in Figure 9(b) show that there is a large increase in Fe concentration at the grain boundary as the overall Fe content in the sample grows.

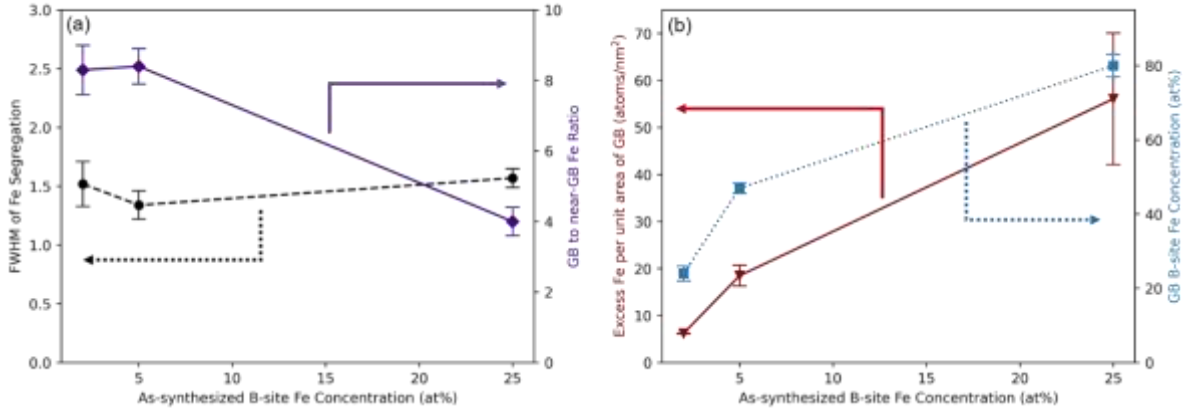

Figure 9: Comparison of Fe segregation behavior between the three Fe containing samples studied. (a) Segregation width (in terms of FWHM of the Fe segregation profile) (a, black circles) does not change based on Fe content on the B-site. However, the GB to near-GB Fe ratio as measured from high resolution mapping (a, purple diamonds) decreases as bulk Fe content increases. (b) The Fe concentration at the GB measured from high-resolution analysis (b, blue squares) increases as bulk Fe content increases. The excess Fe measured using the spatial difference method from low-resolution analysis (b, red triangles) shows the same trend.

In addition to comparing data from high-resolution maps, the spatial difference method can be used to quantify grain boundary excess for low-resolution maps [70,71]. The spatial difference analysis allows for more grain boundaries to be analyzed (three, five, and six GBs for the 2%, 5%, and 25% Fe containing samples, respectively), and shows an identical trend to what has been observed in high-resolution analysis (Figure 9(b)). The spatial difference method was also used to quantify the level of Ti depletion at GBs in the three samples, displaying a trend which is the inverse of the trend in Fe segregation (see Figure S10). The data presented in Figure 9 is summarized in Table 3.

Table 3: Summary of Fe segregation behavior measured for the three Fe-containing samples analyzed.

As-synthesized Fe content (B-site at%)	FWHM of Fe Segregation (nm)	GB to near-GB Fe intensity ratio	GB B-site Fe conc. (at %)	Fe Excess at GB (atoms/nm^2)
2	1.52 ± 0.19	8.3 ± 0.7	24 ± 2	6.2 ± 0.1
5	1.34 ± 0.12	8.4 ± 0.5	47 ± 1	18.5 ± 2.2
25	1.57 ± 0.08	4.0 ± 0.4	80 ± 3	56.1 ± 14.0

4. Discussion

The results in this work present a detailed analysis of grain boundary segregation at general grain boundaries in STF as the Fe content is changed. Variations in local material chemistry as a function of Fe content are observed, both at low resolution and at high resolution. At low resolution, all Fe containing samples show Fe segregation at grain boundaries. For low Fe contents (undoped and 2% Fe), the samples look to be homogeneous at a larger length-scale (as seen in Figures 2(a) and 3(a)), but once the Fe content increases above the dilute limit (5% and 25% Fe), significant inhomogeneity is observed in the B-site cation distribution within individual grains (Figures 4(a) and 5(a)). In both the 5% and the 25% Fe containing samples, some grain boundaries are observed to have symmetrical segregation, in which the Fe signal at the GB is increased, with a depleted region on either side. Several boundaries are also observed in each sample which border sections of grains with increased or depleted Fe content. The origin of this inhomogeneity in Fe segregation within grains is unknown, but is expected to be a result of kinetic limitations. The simplest explanation for the patches of higher Fe content observed in Figures 4(a) and 5(a) is that a solute-drag effect is present, which would explain why the regions of higher Fe content tend to reside in the center of the grains. Inhomogeneities in the B-site cation distribution will have an impact on the conductivity of the samples, causing local inhomogeneities in charge transport correlating to the regions with varying Fe content. As a result, the impedance of the 5% and 25% Fe samples will be impacted, likely resulting in a distortion in the bulk semicircle.

As Fe content increases, the Ti signal at grain boundaries decreases, moving from increased Ti at the GB in the undoped sample to no obvious depletion or segregation of Ti in the 2% Fe sample, and finally to clear Ti depletion in both the 5% and 25% Fe samples (Figure S10). In addition to changes in B-site chemistry, there is Sr depletion observed at the grain boundary in all four samples,

which does not change significantly as Fe content is varied. Grain boundary segregation widths are consistent among Fe-containing samples, but there are large variations in Fe distribution within grains once the Fe content moves above the dilute solute limit. STF is generally accepted to be a solid-solution between two end compounds (strontium titanate and strontium ferrite), however there is significant inhomogeneity in the B-site cation distribution in Figures 4(a) and 5(a). The inhomogeneity in B-site cation distributions could be a result of a barrier to a complete intermixing (i.e. a miscibility gap is present), or it could be a kinetic effect resulting from incomplete mixing during processing. The EDS linescan in Figure 5(b) suggests that the Fe content within the grains of the 25% Fe sample ranges from ~20 at% (on the B-site) to ~35 at%, a significant but less drastic variation than the segregation which is observed at the grain boundaries, where the average Fe content was measured to be 80% (Table 3).

The grain boundary segregation behavior observed at low resolution generally fits with the behavior which is expected for Fe doped strontium titanate based on conventional space charge theory [21,23]; the behavior can be explained as a result of the positively charged grain boundary core attracting negatively charged defects (V_{Sr}'' and Fe_{Ti}') to the space charge region. In addition, Fe segregation profile widths at low resolution fit well with what is expected for space charge layers in strontium titanate [18,25,41,80], ranging in width from ~5-35 nm depending on the sample (Table S2) There is also good agreement between the low-resolution analysis in this study to preceding work with comparable spatial resolution [44]. The spatial difference method used on low-resolution data shows a large increase in Fe excess at grain boundaries as the bulk Fe content increases (Figure 9, Table S3).

At high resolution the Fe segregation is shown to be much thinner than can be detected at low resolution, with Figure 9(a) showing that all three Fe containing samples have GB segregation widths around 1.5 nm or less. The low-resolution EDS mapping will less accurate because of the larger pixel sizes and imprecise beam positioning as compared to the high-resolution mappings. Additionally, at high resolution it becomes clear that all Fe containing samples have significant Fe segregation at the GB core, an effect which is also not resolved with lower resolution analysis. The observation of Fe segregation at the GB core is incongruous with classic space charge models, which typically operate

under the assumption that acceptor dopants segregate to the space charge region, but not the GB core itself [21,22]. The length-scale of Fe segregation in all samples studied further highlights that there is a clear discrepancy between continuum models for space charge segregation and the atomistic nature of ionic segregation profiles at GBs in the STF system.

It was anticipated that the transition from a near-dilute solution (the 2% Fe sample) to a highly concentrated solution (the 25% Fe sample) would bring with it a significant change in segregation behavior [33,49,50], however there is no notable difference in Fe segregation widths between the three Fe-containing samples (Figure 9(a)). In the case of STF, the dilute to concentrated solid solution transition does not greatly impact Fe segregation behavior at grain boundaries. While Fe segregation widths do not change, the Fe concentration within the grain boundary increases greatly as the sample Fe content is raised (Figure 9(b)). In certain systems (such as Ca doped ceria), the grain boundary can become saturated with dopant [81], but this is not observed in the compositional range studied in this work.

Electrochemical impedance spectroscopy shows that the addition of Fe results in an increase in sample conductivity. The observations of Fe segregation behavior made here emphasize the importance of high spatial resolution analysis, without which much of the detail about GB chemistry in STF would remain hidden. The consistent trends in cationic segregation behavior across samples which were processed in a variety of ways is an indication that the effects observed in this work are not due to the specific processing methods used; instead, the segregation behavior is expected to be inherent to strontium ferrite – strontium titanate solid solutions.

Space charge layers at grain boundaries were indirectly measured by EIS in Figure 1. A comparison of the calculated Mott-Schottky (MS) barrier widths (Table 1) indicates that the electrochemical width of the grain boundaries decreases as Fe is added to the system. Space charge widths would be expected to continue to decrease when moving from the 2 % Fe containing sample to the 5 % and 25 % Fe containing samples. However, there is no difference in Fe segregation widths between the three Fe containing samples. The absence of variation in Fe segregation widths for the three samples suggests that Fe segregation in STF is decoupled from the space charge layers at the

boundary. One explanation for the decoupling of segregation and space charge is that the space charge region collapses at the sintering temperature, at which point the cations are highly mobile. However, other charge carriers can continue to equilibrate as the sample is cooled after sintering, causing a space charge layer to form which is not reflected in the cationic segregation profile. Usler et al. have examined this type of 'restricted equilibrium' space charge model for ceria, showing that it fits to the real behavior better than the simplified Mott-Schottky model [29]. All Fe-containing samples show Fe segregation to the grain boundaries, and a higher Fe content results in a higher Fe concentration at the GB (Figure 9(b)). Impedance spectroscopy (Figure 1) clearly shows a drastic increase in conductivity as Fe content increases, and activation energies for grain boundary and bulk conductivities decrease when going from undoped to 2% Fe doped strontium titanate (Table 1).

The conventional defect chemical approach to understanding space charge in Fe doped strontium titanate is to consider Fe as an acceptor dopant [21,25]. However, once the Fe content in the sample increases above the dilute limit, taking Fe as an acceptor dopant ceases to be a logical approach. It stands to reason that, near the dilute limit (i.e. 2% Fe), the segregation of Fe (an acceptor) to the GB core results in a reduction of the GB core charge. However, for Fe contents above the dilute solution limit, Fe contents estimated around 80% on the B-site are present, a composition where Fe cannot be considered a dopant species. In the literature, it has been argued that Fe (and some oxygen vacancies) should be considered part of the STF host lattice (which is assumed to be inherently ordered and oxygen deficient) [34,35,82]. As a result, the effect of Fe segregation on the charge of the GB core (and also the space charge layer) is not obvious, particularly at the higher Fe concentrations (5% and 25% Fe) analyzed in this work. EELS analysis of the 25% Fe doped sample (Figure 7) was performed to help understand the electronic environment resulting from Fe segregation to the grain boundary. The structure of the Ti and O edges in Figure 7 fit well with what is typically seen for grain boundaries in strontium titanate [77], suggesting that the chemical bonding environment at grain boundaries is not highly impacted by the significant Fe segregation. Due to the relatively low EELS signal for Fe within the grain interior, it could not be determined conclusively whether a change in Fe valency occurs at the grain boundary.

In the case of the 25% Fe sample, there is a large excess of Fe at the grain boundary. The HRSTEM/EDS map in Figure 5(d) shows that Fe replaces Ti on the B-site on the two atomic planes adjacent to the grain boundary. Additionally, the Fe segregation clearly follows the faceting of the grains at the GB. A comparison of the experimental result with the STEM/EDS simulations presented in Figure 8 suggest that a significant amount of Fe is also present at the grain boundary core, and that there may be some Fe sitting on the A-site of the perovskite, which would explain the high values for Fe excess calculated by the spatial difference method (Table 3). There are additional effects which could have an impact on the experimental result, such as some disorder in the atomic positions, or steps in the grain boundary through the thickness of the lamella. The propensity of Fe to sit on the A-site is also an explanation for why STF is often synthesized to be Sr-deficient, as it is in this work.

At the current stage, there are multiple explanations for the high concentration of Fe present at the grain boundaries in all of the Fe-containing samples. One plausible conclusion is that Fe segregation occurs through a solute-drag effect, where Fe is collected at the grain boundary during sintering. Zahler et al. [44] have provided experimental evidence for solute drag in STF samples with lower Fe contents (2% and 5%), indicating that solute drag could be a factor in the segregation behavior. The segregation could be a thermodynamic effect, either through a complexion transition, through an elastic mismatch effect, or by an electrostatic-driven segregation process [83,84]. The samples in this work show varying Fe contents at the grain boundaries (Figure 9(b)), dependent on the bulk Fe content, but look to have an equilibrium segregation width. Additionally, no structural changes at the grain boundary are observed, so it remains unclear whether the segregation is best described as a result of complexion formation.

At the higher Fe concentrations, there is a fundamental question about what drives Fe to segregate at the grain boundary core versus to the crystal lattice on the first planes adjacent to the GB. The GB segregation process can be driven by two separate effects simultaneously; for instance, Fe can segregate to the disordered GB plane as an adsorbate which reduces interfacial energy, after which additional Fe segregates to the lattice adjacent to the GB due to space-charge effects. On the other

hand, GB segregation may have a sole driving force, which is strong enough to saturate the GB plane with Fe and propel additional Fe to the grain directly adjacent to the GB.

While the current work is heavily focused on chemical segregation at grain boundaries in the material, the structure of grain boundaries will have a large impact on their properties. All of the boundaries studied in this work are 'general' grain boundaries, with a variety of grain and grain boundary plane orientations (though each GB selected was able to be aligned edge-on while one grain was oriented to a low-index zone axis). As a result, grain boundary structures will vary widely, as has been shown in a variety of work on strontium titanate in the literature [32,77,85]. When analyzing chemical segregation, segregation widths are fairly consistent among the grain boundaries which were studied (Table 2, Figure 9(a)). In the case of the 25% Fe sample, atomic resolution EDS mapping (Figure 5(d)) actually shows that Fe segregation mirrors the faceting of the boundary, with columns closest to the boundary containing the highest apparent Fe content. The results from all of the Fe containing samples illustrate that there is a discrepancy between continuum models currently used for descriptions of space charge, and the clearly atomistic nature of grain boundary segregation in STF. Fe is segregated to within 1-2 atomic planes of the grain boundary in all Fe contents which were analyzed, at which point the atomistic characteristics of grain boundary segregation become significant to an understanding of grain boundary segregation behavior.

5. Conclusions

In the current work, STEM has been utilized to comprehensively characterize grain boundary chemistry in strontium titanate-ferrite at a variety of Fe levels, ranging from near the dilute limit (2% Fe on the B-site), to well above the dilute limit (25% Fe). Cationic segregation was probed at both low and high resolution, showing that Fe segregation behavior is remarkably consistent across the dopant range which was studied. Fe is clearly segregated to the grain boundary core in all Fe-containing samples, and Fe segregation widths remain around 1.5 nm in all samples. The concentration of Fe which is segregated at the GB is shown to increase with increasing bulk Fe content, to the point where the Fe content is measured to be 87% on the B-site at the grain boundaries of the 25% Fe containing sample. In addition, Sr depletion is observed at the grain boundaries in all samples, and Ti depletion at

the grain boundaries is present at higher Fe contents (as Fe is replacing Ti on the B-site). Impedance spectroscopy showed that sample conductivity increases as Fe content increases. The unvarying Fe segregation widths run contrary to expectations of segregation behavior as the overall Fe content is altered. In total, the results in this work demonstrate the importance of high spatial resolution analysis when attempting to understand the impacts of material doping on grain boundary chemistry. Also shown are significant discrepancies between the classic continuum models for space charge-driven segregation in strontium titanates and the atomistic nature of cationic segregation and depletion at grain boundaries in STF.

6. Acknowledgements

The authors have no competing interests to declare. The authors wish to thank Dr. Doris Sebold for assistance with SEM image acquisition. The authors acknowledge the support of Hitachi High-Technologies in providing access to and expertise for the HF5000 STEM. Funding for this work was provided by the Deutsche Forschungsgemeinschaft via the Emmy Noether Programme (Rh 146/1-1.), MA 1280/69–1 (MK, OG), and within the SFB 1548 FLAIR (B04, 463184206).

References:

[1] K.D. Kreuer, Proton-Conducting Oxides, Annu. Rev. Mater. Res. 33 (2003) 333–59. https://doi.org/10.1146/annurev.matsci.33.022802.091825.

[2] K. Bae, D.Y. Jang, H.J. Choi, D. Kim, J. Hong, B.K. Kim, J.H. Lee, J.W. Son, J.H. Shim, Demonstrating the potential of yttrium-doped barium zirconate electrolyte for high-performance fuel cells, Nat. Commun. 8 (2017) 1–9. https://doi.org/10.1038/ncomms14553.

[3] Z. Shao, W. Yang, Y. Cong, H. Dong, J. Tong, G. Xiong, Investigation of the permeation behavior and stability of a $Ba0.5Sr0.5Co_{0.8}Fe_{0.2}O_{3-\delta}$ oxygen membrane, J. Memb. Sci. 172 (2000) 177–188. https://doi.org/10.1016/S0376-7388(00)00337-9.

[4] B.C.H. Steele, Oxygen ion conductors and their technological applications, Mater. Sci. Eng. B. 13 (1992) 79–87. https://doi.org/10.1016/0921-5107(92)90146-Z.

[5] M. Morgenbesser, A. Schmid, A. Viernstein, J. de Dios Sirvent, F. Chiabrera, N. Bodenmüller, S. Taibl, M. Kubicek, F. Baiutti, A. Tarancon, J. Fleig, SrTiO$_3$ based high temperature solid oxide solar cells: Photovoltages, photocurrents and mechanistic insight, Solid State Ionics. 368 (2021) 115700. https://doi.org/10.1016/j.ssi.2021.115700.

[6] J. Gerblinger, H. Meixner, Fast oxygen sensors based on sputtered strontium titanate, Sensors Actuators B Chem. 4 (1991) 99–102. https://doi.org/10.1016/0925-4005(91)80183-K.

[7] L. Yang, K. Xie, S. Xu, T. Wu, Q. Zhou, T. Xie, Y. Wu, Redox-reversible niobium-doped strontium titanate decorated with in situ grown nickel nanocatalyst for high-temperature direct steam electrolysis, 43 (2014) 14147. https://doi.org/10.1039/c4dt01430h.

[8] G. Neri, A. Bonavita, G. Micali, G. Rizzo, R. Licheri, R. Orrù, G. Cao, Resistive λ-sensors based on ball milled Fe-doped SrTiO$_3$ nanopowders obtained by self-propagating high-temperature synthesis (SHS), Sensors Actuators, B Chem. 126 (2007) 258–265. https://doi.org/10.1016/J.SNB.2006.12.008.

[9] V. V. Kharton, A. V. Kovalevsky, A.P. Viskup, J.R. Jurado, F.M. Figueiredo, E.N. Naumovich, J.R. Frade, Transport properties and thermal expansion of Sr$_{0.97}$Ti$_{1-x}$Fe$_x$O$_{3-\delta}$ (x = 0.2-0.8), J. Solid State Chem. 156 (2001) 437–444. https://doi.org/10.1006/JSSC.2000.9019.

[10] A. Rothschild, W. Menesklou, H.L. Tuller, E. Ivers-Tiffée, Electronic structure, defect chemistry, and transport properties of SrTi$_{1-x}$Fe$_x$O$_{3-y}$ solid solutions, Chem. Mater. 18 (2006) 3651–3659. https://doi.org/10.1021/CM052803X/ASSET/IMAGES/LARGE/CM052803XF00011.JPEG.

[11] B.E. Hayden, F.K. Rogers, Oxygen reduction and oxygen evolution on SrTi$_{1−x}$Fe$_x$O$_{3−y}$ (STFO) perovskite electrocatalysts, J. Electroanal. Chem. 819 (2018) 275–282. https://doi.org/10.1016/J.JELECHEM.2017.10.056.

[12] V. Metlenko, W. Jung, S.R. Bishop, H.L. Tuller, R.A. De Souza, Oxygen diffusion and surface exchange in the mixed conducting oxides SrTi$_{1−y}Fe$_{y}O$_{3−/delta}$, Phys. Chem. Chem. Phys. 18 (2016) 29495–29505. https://doi.org/10.1039/C6CP05756J.

[13] S. Steinsvik, Y. Larring, T. Norby, Hydrogen ion conduction in iron-substituted strontium titanate, SrTi1-xFexO3-x/2 ($0 \leq x \leq 0.8$), Solid State Ionics. 143 (2001) 103–116. https://doi.org/10.1016/S0167-2738(01)00838-4.

[14] W.C. Jung, H.L. Tuller, Impedance study of SrTi$_{1-x}Fe$_{x}O_{3-/delta}$ (x = 0.05 to 0.80) mixed ionic-electronic conducting model cathode, Solid State Ionics. 180 (2009) 843–847. https://doi.org/10.1016/j.ssi.2009.02.008.

[15] W.C. Jung, H.L. Tuller, Investigation of Cathode Behavior of Model Thin-Film SrTi$_{1−x}Fe$_{x}O$_{3−/delta} (x = 0.35 and 0.5) Mixed Ionic-Electronic Conducting

Electrodes, J. Ele. (2008) B1194–B1201. https://doi.org/10.1149/1.2976212.

[16] F. Schulze-Küppers, S.F.P. Ten Donkelaar, S. Baumann, P. Prigorodov, Y.J. Sohn, H.J.M. Bouwmeester, W.A. Meulenberg, O. Guillon, Structural and functional properties of SrTi$_{1−x}$Fe$_x$O$_{3−/delta}$ (0⩽x⩽1) for the use as oxygen transport membrane, Sep. Purif. Technol. 147 (2015) 414–421. https://doi.org/10.1016/J.SEPPUR.2014.12.020.

[17] Y. Liu, S. Baumann, F. Schulze-Küppers, D.N. Mueller, O. Guillon, Co and Fe co-doping influence on functional properties of SrTiO$_3$ for use as oxygen transport membranes, J. Eur. Ceram. Soc. 38 (2018) 5058–5066. https://doi.org/10.1016/j.jeurceramsoc.2018.07.037.

[18] Y. Wu, P.C. Bowes, J.N. Baker, D.L. Irving, Influence of space charge on the conductivity of nanocrystalline SrTiO3, J. Appl. Phys. 128 (2020) 1–10. https://doi.org/10.1063/5.0008020.

[19] V. Ravikumar, R.P. Rodrigues, V.P. Dravid, Space-charge distribution across internal interfaces in electroceramics using electron holography: II, doped grain boundaries, J. Am. Ceram. Soc. 80 (1997) 1131–1138. https://doi.org/10.1111/J.1151-2916.1997.TB02955.X.

[20] M. Shirpour, B. Rahmati, W. Sigle, P.A. Van Aken, R. Merkle, J. Maier, Dopant Segregation and Space Charge Effects in Proton-Conducting BaZrO$_3$ Perovskites, J. Phys. Chem. C. 116 (2012) 2453–2461. https://doi.org/10.1021/jp208213x.

[21] R.A. De Souza, The formation of equilibrium space-charge zones at grain boundaries in the perovskite oxide SrTiO3, Phys. Chem. Chem. Phys. 11 (2009) 9939–9969. https://doi.org/10.1039/b904100a.

[22] G. Gregori, R. Merkle, J. Maier, Ion conduction and redistribution at grain boundaries in oxide systems, Prog. Mater. Sci. 89 (2017) 252–305. https://doi.org/10.1016/j.pmatsci.2017.04.009.

[23] Y. -M Chiang, T. Takagi, Grain-Boundary Chemistry of Barium Titanate and Strontium Titanate: I, High-Temperature Equilibrium Space Charge, J. Am. Ceram. Soc. 73 (1990) 3278–3285. https://doi.org/10.1111/J.1151-2916.1990.TB06450.X.

[24] M. Leonhardt, J. Jamnik, J. Maier, In Situ Monitoring and Quantitative Analysis of Oxygen Diffusion Through Schottky-Barriers in SrTiO$_3$ Bicrystals, Electrochem. Solid-State Lett. 2 (1999) 333–335.

[25] M. Vollman, R. Waser, Grain Boundary Defect Chemistry of Acceptor-Doped Titanates: Space Charge Layer Width, J. Am. Ceram. Soc. 77 (1994) 235–243. https://doi.org/10.1111/J.1151-2916.1994.TB06983.X.

[26] I. Denk, J. Claus, J. Maier, Electrochemical Investigations of SrTiO3 Boundaries, J. Electrochem. Soc. 144 (1997) 3526–3536.

[27] F.A. Kröger, H.J. Vink, Relations between the Concentrations of Imperfections in Crystalline Solids, Solid State Phys. - Adv. Res. Appl. 3 (1956) 307–435. https://doi.org/10.1016/S0081-1947(08)60135-6.

[28] J. Jamnik, J. Maier, S. Pejovnik, Interfaces in solid ionic conductors: Equilibrium and small signal picture, Solid State Ionics. 75 (1995) 51–58. https://doi.org/10.1016/0167-2738(94)00184-T.

[29] A.L. Usler, R.A. De Souza, A Critical Examination of the Mott–Schottky Model of Grain-Boundary Space-Charge Layers in Oxide-Ion Conductors, J. Electrochem. Soc. 168 (2021) 1–11. https://doi.org/10.1149/1945-7111/ABFB37.

[30] S. Kim, J. Fleig, J. Maier, Space charge conduction: Simple analytical solutions for ionic and mixed conductors and application to nanocrystalline ceria, Phys. Chem. Chem. Phys. 5 (2003) 2268–2273. https://doi.org/10.1039/B300170A.

[31] X. Tong, D.S. Mebane, R.A. De Souza, Analyzing the grain-boundary resistance of oxide-ion

conducting electrolytes: Poisson-Cahn vs Poisson-Boltzmann theories, J. Am. Ceram. Soc. 103 (2020) 5–22. https://doi.org/10.1111/JACE.16716.

[32] S. von Alfthan, N.A. Benedek, L. Chen, A. Chua, D. Cockayne, K.J. Dudeck, C. Elsässer, M.W. Finnis, C.T. Koch, B. Rahmati, M. Ruhle, S.-J. Shih, A.P. Sutton, The Structure of Grain Boundaries in Strontium Titanate: Theory, Simulation, and Electron Microscopy, Annu. Rev. Mater. Res. (2010) 557–599. https://doi.org/10.1146/annurev-matsci-010510-104604.

[33] X. Tong, W.J. Bowman, A. Mejia-Giraldo, P.A. Crozier, D.S. Mebane, New Data-Driven Interacting-Defect Model Describing Nanoscopic Grain Boundary Compositions in Ceramics, J. Phys. Chem. C. 124 (2020) 23619–23625. https://doi.org/10.1021/ACS.JPCC.0C05713.

[34] R. Bredesen, T. Norby, A. Bardal, V. Lynum, Phase relations, chemical diffusion and electrical conductivity in pure and doped Sr$_4$Fe$_6$O$_13$ mixed conductor materials, Solid State Ionics. 135 (2000) 687–697. https://doi.org/10.1016/S0167-2738(00)00382-9.

[35] T. Norby, Fast oxygen ion conductors—from doped to ordered systems, J. Mater. Chem. 11 (2001) 11–18. https://doi.org/10.1039/B003463K.

[36] N. Kim, N.H. Perry, E. Ertekin, Atomic Modeling and Electronic Structure of Mixed Ionic-Electronic Conductor SrTi$_{1-x}Fe$_xO_{3-x/2+\delta} Considered as a Mixture of SrTiO$_3$ and Sr$_2$Fe$_2$O$_5$, Chem. Mater. 31 (2019) 233–243. https://doi.org/10.1021/ACS.CHEMMATER.8B04284/ASSET/IMAGES/LARGE/CM-2018-04284J_0008.JPEG.

[37] N. Kim, B.J. Blankenau, T. Su, N.H. Perry, E. Ertekin, Multisublattice cluster expansion study of short-range ordering in iron-substituted strontium titanate, Comput. Mater. Sci. (2022) 110969. https://doi.org/10.1016/j.commatsci.2021.110969.

[38] Y.G. Wang, S. Steinsvik, R. Hoier, T. Norby, Annealing effect on microstructure of iron-substituted strontium titanate revealed by high resolution transmission electron microscopy, J. Mater. Sci. Lett. (1995) 1027–1029.

[39] S. Steinsvik, R. Bugge, J. Gjønnes, J. Taftø, T. Norby, THE DEFECT STRUCTUFE OF SrTi1−xFexO3−y (x = 0–0.8) INVESTIGATED BY ELECTRICAL CONDUCTIVITY MEASUREMENTS AND ELECTRON ENERGY LOSS SPECTROSCOPY (EELS), J. Phys. Chem. Solids. 58 (1997) 969–976. https://doi.org/10.1016/S0022-3697(96)00200-4.

[40] L.H. Brixner, Preparation and properties of the SrTi$_{1−x}Fe$_xO_{3−x2}$/O$_{x2}$ system, Mater. Res. Bull. 3 (1968) 299–308. https://doi.org/10.1016/0025-5408(68)90001-9.

[41] N. Wilcox, V. Ravikumar, R.P. Rodrigues, V.P. Dravid, M. Vollmann, R. Waser, K.K. Soni, A.G. Adriaens, Investigation of grain boundary segregation in acceptor and donor doped strontium titanate, Solid State Ionics. 75 (1995) 127–136. https://doi.org/10.1016/0167-2738(94)00221-D.

[42] S.M. Wang, S.J.L. Kang, Grain Boundary Segregation and High Nonlinear I–V Characteristics in Fe-Added Strontium Titanate, J. Am. Ceram. Soc. 91 (2008) 2617–2622. https://doi.org/10.1111/J.1551-2916.2008.02532.X.

[43] R.A. De Souza, J. Fleig, J. Maier, O. Kienzle, Z. Zhang, W. Sigle, M. Rühle, Electrical and structural characterization of a low-angle tilt grain boundary in iron-doped strontium titanate, J. Am. Ceram. Soc. 86 (2003) 922–928. https://doi.org/10.1111/J.1151-2916.2003.TB03398.X.

[44] M.P. Zahler, S.M. Kraschewski, H. Störmer, D. Gerthsen, M. Bäurer, W. Rheinheimer, Grain growth and segregation in Fe-doped SrTiO3: Experimental evidence for solute drag, J. Eur. Ceram. Soc. 43 (2023) 1613–1624. https://doi.org/10.1016/j.jeurceramsoc.2022.11.074.

[45] T.P. Mishra, S. Wang, C. Lenser, D. Jennings, M. Kindelmann, W. Rheinheimer, C. Broeckmann, M. Bram, O. Guillon, Ultra-fast high temperature sintering of strontium titanate, Acta Mater. 231 (2022).

[46] W.J. Bowman, A. Darbal, P.A. Crozier, Linking Macroscopic and Nanoscopic Ionic Conductivity: A Semiempirical Framework for Characterizing Grain Boundary Conductivity in Polycrystalline Ceramics, ACS Appl. Mater. Interfaces. (2020) 507–517. https://doi.org/10.1021/acsami.9b15933.

[47] G.L. Burton, S. Ricote, B.J. Foran, D.R. Diercks, B.P. Gorman, Quantification of grain boundary defect chemistry in a mixed proton-electron conducting oxide composite, J. Am. Ceram. Soc. 103 (2020) 3217–3230. https://doi.org/10.1111/JACE.17014.

[48] W.J. Bowman, J. Zhu, R. Sharma, P.A. Crozier, Electrical conductivity and grain boundary composition of Gd-doped and Gd/Pr co-doped ceria, Solid State Ionics. 272 (2015) 9–17. https://doi.org/10.1016/J.SSI.2014.12.006.

[49] D.S. Mebane, R.A. De Souza, A generalised space-charge theory for extended defects in oxygen-ion conducting electrolytes: from dilute to concentrated solid solutions, Energy Environ. Sci. 8 (2015) 2935–2940. https://doi.org/10.1039/c5ee02060c.

[50] X. Tong, D.S. Mebane, Kinetic modeling of near-interface defect segregation during thermal annealing of oxygen-conducting solid electrolytes, Solid State Ionics. 299 (2017) 78–81. https://doi.org/10.1016/j.ssi.2016.08.008.

[51] W. Deibert, M.E. Ivanova, K. Ran, J. Mayer, W.A. Meulenberg, Up-scaling and processing related characterisation of hydrogen permeation membranes based on pristine and Mo substituted La28−xW4+xO54+1.5x, J. Eur. Ceram. Soc. 43 (2023) 121–129. https://doi.org/10.1016/j.jeurceramsoc.2022.09.033.

[52] W. Deibert, M.E. Ivanova, Y. Huang, R. Merkle, J. Maier, W.A. Meulenberg, Fabrication of multi-layered structures for proton conducting ceramic cells, J. Mater. Chem. A. 10 (2022) 2362–2373. https://doi.org/10.1039/d1ta05240c.

[53] W. Deibert, M.E. Ivanova, W.A. Meulenberg, R. Vaßen, O. Guillon, Preparation and sintering behaviour of La5.4WO12-δ asymmetric membranes with optimised microstructure for hydrogen separation, J. Memb. Sci. 492 (2015) 439–451. https://doi.org/10.1016/j.memsci.2015.05.065.

[54] M.P. Zahler, D. Jennings, M. Kindelmann, O. Guillon, W. Rheinheimer, Reactive FAST/SPS sintering of strontium titanate as a tool for grain boundary engineering, J. Eur. Ceram. Soc. (2023). https://doi.org/10.1016/j.jeurceramsoc.2023.07.021.

[55] J.E. Bauerle, Study of solid electrolyte polarization by a complex admittance method, Solid State Commun. 7 (1969) 2657–2670. https://doi.org/10.1016/0038-1098(69)90484-0.

[56] S.M. Haile, D.L. West, J. Campbell, The role of microstructure and processing on the proton conducting properties of gadolinium-doped barium cerate, J. Mater. Res. 13 (2011) 1576–1595.

[57] J.C.C. Abrantes, J.A. Labrincha, J.R. Frade, Applicability of the brick layer model to describe the grain boundary properties of strontium titanate ceramics, J. Eur. Ceram. Soc. 20 (2000) 1603–1609. https://doi.org/10.1016/S0955-2219(00)00022-4.

[58] D.M. Smyth, The Defect Chemistry of Metal Oxides, 2000.

[59] R.A. De Souza, J. Fleig, R. Merkle, J. Maier, SrTiO3: A model electroceramic, Int. J. Mater. Res. 94 (2003) 218–225. https://doi.org/10.3139/146.030218.

[60] J. Fleig, S. Rodewald, J. Maier, Microcontact impedance measurements of individual highly conductive grain boundaries: General aspects and application to acceptor-doped SrTiO$_3$, J. Appied Phys. 87 (2000) 2372–2381. https://doi.org/10.1039/a902839k.

[61] A. Kovács, R. Schierholz, K. Tillman, FEI Titan G2 80-200 CREWLEY, J. Large-Scale Res. Facil. (2016) 1–4. https://doi.org/10.17815/jlsrf-2-68.

[62] M. Kruth, D. Meertens, K. Tillmann, FEI Helios NanoLab 460F1 FIB-SEM, J. Large-Scale Res. Facil. 2 (2016) 1–4. https://doi.org/10.17815/JLSRF-2-105.

[63] F. de la Peña, E. Prestat, V.T. Fauske, P. Burdet, J. Lähnemann, P. Jokubauskas, T. Furnival, M. Nord, T. Ostasevicius, K.E. MacArthur, D.N. Johnstone, M. Sarahan, J. Taillon, T. Aarholt, V. Migunov, A. Eljarrat, J. Caron, C. Francis, T. Nemoto, T. Poon, S. Mazzucco, N. Tappy, N. Cautaerts, S. Somnath, T. Slater, M. Walls, F. Winkler, H.W. Ånes, hyperspy/hyperspy: Release v1.7.2, (2022). https://doi.org/10.5281/ZENODO.7090040.

[64] K.E. MacArthur, H.G. Brown, S.D. Findlay, L.J. Allen, Probing the effect of electron channelling on atomic resolution energy dispersive X-ray quantification, Ultramicroscopy. 182 (2017) 264–275. https://doi.org/10.1016/J.ULTRAMIC.2017.07.020.

[65] H. Hoeft, P. Schwaab, Investigations towards optimizing EDS analysis by the Cliff-Lorimer method in scanning transmission electron microscopy, X-Ray Spectrom. 17 (1988) 201–208. https://doi.org/10.1002/XRS.1300170509.

[66] A. Molinari, R. Witte, K.K. Neelisetty, S. Gorji, C. Kübel, I. Münch, F. Wöhler, L. Hahn, S. Hengsbach, K. Bade, H. Hahn, R. Kruk, Configurable Resistive Response in BaTiO3 Ferroelectric Memristors via Electron Beam Radiation, Adv. Mater. 32 (2020) 1–7. https://doi.org/10.1002/adma.201907541.

[67] K.K. Neelisetty, X. Mu, S. Gutsch, A. Vahl, A. Molinari, F. Von Seggern, M. Hansen, T. Scherer, M. Zacharias, L. Kienle, V.S.K. Chakravadhanula, C. Kübel, Electron Beam Effects on Oxide Thin Films — Structure and Electrical Property Correlations, Microsc. Microanal. (2019) 592–600. https://doi.org/10.1017/S1431927619000175.

[68] H. Du, A nonlinear filtering algorithm for denoising HR(S)TEM micrographs, Ultramicroscopy. 151 (2015) 62–67. https://doi.org/10.1016/J.ULTRAMIC.2014.11.012.

[69] T. Malis, S.C. Cheng, R.F. Egerton, EELS log-ratio technique for specimen-thickness measurement in the TEM, J. Electron Microsc. Tech. 8 (1988) 193–200. https://doi.org/10.1002/JEMT.1060080206.

[70] V.J. Keast, D.B. Williams, Quantification of boundary segregation in the electron microscope, J. Microsc. 199 (2000) 45–55. https://doi.org/10.1046/j.1365-2818.2000.00694.x.

[71] K. Syed, M. Xu, K.K. Ohtaki, D. Kok, K.K. Karandikar, O.A. Graeve, W.J. Bowman, M.L. Mecartney, Correlations of grain boundary segregation to sintering techniques in a three-phase ceramic, Materialia. 14 (2020) 100890. https://doi.org/10.1016/j.mtla.2020.100890.

[72] L.J. Allen, H.G. Brown, A.J. D'Alfonso, S.D. Findlay, B.D. Forbes, muSTEM, (2017).

[73] K. Momma, F. Izumi, VESTA : a Three-Dimensional Visualization System, (2014).

[74] B.J.T.S. Irvine, D.C. Sinclair, A.R. West, Electroceramics: Characterisation by impedance spectroscopy, Adv. Mater. (1990) 132–138.

[75] K.E. Macarthur, A.B. Yankovich, A. Béché, M. Luysberg, H.G. Brown, S.D. Findlay, M. Heggen, L.J. Allen, Optimizing Experimental Conditions for Accurate Quantitative Energy-Dispersive X-ray Analysis of Interfaces at the Atomic Scale, Microsc. Microanal. 27 (2021) 528–542. https://doi.org/10.1017/S1431927621000246.

[76] C. Yang, Y. Wang, W. Sigle, P.A. van Aken, Determination of Grain-Boundary Structure and Electrostatic Characteristics in a SrTiO 3 Bicrystal by Four-Dimensional Electron Microscopy , Nano Lett. 21 (2021) 9138–9145. https://doi.org/10.1021/ACS.NANOLETT.1C02960/SUPPL_FILE/NL1C02960_SI_001.PDF.

[77] H. Du, C.L. Jia, L. Houben, V. Metlenko, R.A. De Souza, R. Waser, J. Mayer, Atomic structure and chemistry of dislocation cores at low-angle tilt grain boundary in SrTiO3 bicrystals, Acta Mater. 89 (2015) 344–351. https://doi.org/10.1016/J.ACTAMAT.2015.02.016.

[78] D.W. Fischer, Molecular-Orbital Interpretation of the Soft X-Ray LII,LIII Emission and Absorption Spectra from Some Titanium and Vanadium Compounds, J. Appied Phys. 41 (1970) 3561–3569.

[79] D.A. Muller, N. Nakagawa, A. Ohtomo, J.L. Grazul, H.Y. Hwang, Atomic-scale imaging of nanoengineered oxygen vacancy profiles in SrTiO3, Nature. 430 (2004) 657–661. https://doi.org/10.1038/nature02756.

[80] S.Y. Chung, S.J.L. Kang, V.P. Dravid, Effect of sintering atmosphere on grain boundary segregation and grain growth in niobium-doped SrTiO3, J. Am. Ceram. Soc. 85 (2002) 2805–2810. https://doi.org/10.1111/J.1151-2916.2002.TB00532.X.

[81] W.J. Bowman, M.N. Kelly, G.S. Rohrer, C.A. Hernandez, P.A. Crozier, Enhanced ionic conductivity in electroceramics by nanoscale enrichment of grain boundaries with high solute concentration, Nanoscale. 9 (2017) 17293–17302. https://doi.org/10.1039/c7nr06941c.

[82] C.A.J. Fisher, M.S. Islam, Defect, protons and conductivity in brownmillerite-structured Ba$_2$In$_2$O$_5$, Solid State Ionics. 118 (1999) 355–363. https://doi.org/10.1016/S0167-2738(98)00391-9.

[83] W.D. Kaplan, D. Chatain, P. Wynblatt, W.C. Carter, A review of wetting versus adsorption, complexions, and related phenomena: the rosetta stone of wetting, J. Mater. Sci. 48 (2013) 5681–5717. https://doi.org/10.1007/s10853-013-7462-y.

[84] M. Tang, W.C. Carter, R.M. Cannon, Diffuse interface model for structural transitions of grain boundaries, Phys. Rev. B. (2006) 1–14. https://doi.org/10.1103/PhysRevB.73.024102.

[85] H. Sternlicht, W. Rheinheimer, R.E. Dunin-Borkowski, M.J. Hoffmann, W.D. Kaplan, Characterization of grain boundary disconnections in SrTiO3 part I: the dislocation component of grain boundary disconnections, J. Mater. Sci. 54 (2019) 3694–3709. https://doi.org/10.1007/S10853-018-3096-4/TABLES/3.